Available online at www.sciencedirect.com
ScienceDirect
Geochimica et Cosmochimica Acta 74 (2010) 2677–2696
Geochimica et Cosmochimica Acta
www.elsevier.com/locate/gca

Deciphering formation processes of banded iron formations from the Transvaal and the Hamersley successions by combined Si and Fe isotope analysis using UV femtosecond laser ablation

Grit Steinhoefel [a,*], Friedhelm von Blanckenburg [a,b], Ingo Horn [a], Kurt O. Konhauser [c], Nicolas J. Beukes [d], Jens Gutzmer [d,e]

[a] *Institut für Mineralogie, Universität Hannover, Callinstr. 3, D-30167 Hannover, Germany*
[b] *Deutsches GeoForschungsZentrum GFZ, Telegrafenberg, D-14473 Potsdam, Germany*
[c] *Department of Earth and Atmospheric Sciences, University of Alberta, Edmonton, Alberta, Canada T6G 2E3*
[d] *Paleoproterozoic Mineralization Research Group, Department of Geology, University of Johannesburg, Auckland Park Kingsway Campus, P.O. Box 524, 2006 Auckland Park, South Africa*
[e] *Department of Mineralogy, TU Bergakademie Freiberg, Brennhausgasse 14, 09596 Freiberg, Germany*

Received 1 January 2009; accepted in revised form 22 January 2010; available online 4 February 2010

Abstract

To investigate the genesis of BIFs, we have determined the Fe and Si isotope composition of coexisting mineral phases in samples from the ~2.5 billion year old Kuruman Iron Formation (Transvaal Supergroup, South Africa) and Dales Gorges Member of the Brockman Iron Formation (Hamersley Group, Australia) by UV femtosecond laser ablation coupled to a MC-ICP-MS. Chert yields a total range of δ^{30}Si between −1.3‰ and −0.8‰, but the Si isotope compositions are uniform in each core section examined. This uniformity suggests that Si precipitated from well-mixed seawater far removed from its sources such as hydrothermal vents or continental drainage. The Fe isotope composition of Fe-bearing mineral phases is much more heterogeneous compared to Si with δ^{56}Fe values of −2.2‰ to 0‰. This heterogeneity is likely due to variable degrees of partial Fe(II) oxidation in surface waters, precipitation of different mineral phases and post-depositional Fe redistribution. Magnetite exhibits negative δ^{56}Fe values, which can be attributed to a variety of diagenetic pathways: the light Fe isotope composition was inherited from the Fe(III) precursor, heavy Fe(II) was lost by abiotic reduction of the Fe(III) precursor or light Fe(II) was gained from external fluids. Micrometer-scale heterogeneities of δ^{56}Fe in Fe oxides are attributed to variable degrees of Fe(II) oxidation or to isotope exchange upon Fe(II) adsorption within the water column and to Fe redistribution during diagenesis. Diagenetic Fe(III) reduction caused by oxidation of organic matter and Fe redistribution is supported by the C isotope composition of a carbonate-rich sample containing primary siderite. These carbonates yield δ^{13}C values of ~−10‰, which hints at a mixed carbon source in the seawater of both organic and inorganic carbon. The ancient seawater composition is estimated to have a minimum range in δ^{56}Fe of −0.8‰ to 0‰, assuming that hematite and siderite have preserved their primary Fe isotope signature. The long-term near-zero Fe isotope composition of the Hamersley and Transvaal BIFs is in balance with the assumed composition of the Fe sources. The negative Fe isotope composition of the investigated BIF samples, however, indicates either a perturbation of the steady state, or they have to be balanced spatially by deposition of isotopically heavy Fe. In the case of Si, the negative Si isotope signature of these BIFs stands in marked contrast to the assumed source composition. The deviation from potential source composition requires a complementary sink of isotopically heavy Si in order to maintain steady state in the basin. Perturbing the steady state by extraordinary hydrothermal activity or continental weathering in contrast would have led to precipitation of light Si isotopes from seawater. Combining an explanation for both elements, a likely scenario is a steady state ocean basin with two sinks. When all published

* Corresponding author. Tel.: +49 (0) 331 28601.
E-mail address: g.steinhoefel@mineralogie.uni-hannover.de (G. Steinhoefel).

0016-7037/$ - see front matter
doi:10.1016/j.gca.2010.01.028

Fe isotope records including BIFs, microbial carbonates, shales and sedimentary pyrites, are considered, a complementary sink for heavy Fe isotopes must have existed in Precambrian ocean basins. This Fe sink could have been pelagic sediments, which however are not preserved. For Si, such a complementary sink for heavy Si isotopes might have been provided by other chert deposits within the basin.

1. INTRODUCTION

Banded iron formations (BIFs) are prominent chemical marine sediments of Precambrian age whose peak of deposition between 2.3 and 2.5 Ga encompasses a period of dramatic change in the form of the evolution of first large scale microbial activity and the associated change in the atmospheric and ocean chemistry (e.g. Canfield, 2005). Typically, BIFs contain total Fe of 20–40 wt.% and SiO_2 of 43–56 wt.% (Klein, 2005) and are characterized by alternating Fe-rich and Si-rich layers. Therefore, these sediments represent an extraordinary record of the ancient Fe and Si cycles, which are poorly understood but clearly different from those of the Phanerozoic.

The formation of Fe oxide layers is interpreted to reflect periods of intensive upwelling of Fe(II)-rich deep waters or hydrothermal plumes into the oxygenated surface layers of a largely anoxic ocean, which in turn led to the precipitation of a ferric oxyhydroxide precursor (e.g. Klein and Beukes, 1989; Isley, 1995; Beukes and Gutzmer, 2008). Rare earth element (REE) patterns with positive Eu anomalies and mantle-like Nd isotope signatures reveal a predominately hydrothermal origin for Fe (e.g. Jacobsen and Pimentel-Klose, 1988; Klein and Beukes, 1989; Alibert and McCulloch, 1993; Bau and Dulski, 1996; Bau et al., 1997). Chert layers likely record periods of hydrothermal quiescence and Fe-poor sedimentation (e.g. Morris, 1993). In the absence of silica-secreting organisms in the Precambrian, Si either precipitated directly from Si-saturated seawater in the form of an amorphous silica gel or coprecipitated with Fe by adsorption of dissolved Si onto ferric oxyhydroxide (e.g. Siever, 1992; Fischer and Knoll, 2009). The source of Si in the Precambrian seawater is thought to include supply by hydrothermal fluids and/or continental weathering (Hamade et al., 2003; Maliva et al., 2005). Although Fe and Si have been deposited simultaneously, it is still unclear to what extent they have followed common pathways.

Recent analytical advancements now provide the opportunity to study stable Fe and Si isotopes to decipher the genetic processes of BIFs. Mineral phases were formed and altered during multiple stages of BIF genesis. All of these processes, including primary precipitation from seawater, diagenesis and metamorphism, might be recorded in their Fe or Si isotope signatures. The first combined study of Fe and Si isotopes of the Archean Old Wanderer BIF in the Shurugwi Greenstone Belt (Zimbabwe) revealed correlated Fe and Si isotope signatures interpreted to reflect the dynamics of hydrothermal emanation (Steinhoefel et al., 2009a). Iron isotope compositions alone have been studied on a number of BIFs of various ages and different grades of metamorphism (Johnson et al., 2003, 2008a; Dauphas et al., 2004, 2007; Rouxel et al., 2005; Frost et al., 2007; Whitehouse and Fedo, 2007; Valaas Hyslop et al., 2008; Steinhoefel et al., 2009a). The relevant fractionation factors are beginning to be established (see overview in Steinhoefel et al. (2009a)), which facilitates the exploration of the formation pathways of Fe-bearing mineral phases. Specifically, investigations of the voluminous ~2.5 Ga BIFs of the Hamersley and Transvaal successions have revealed large variations in Fe isotope composition (Johnson et al., 2003, 2008a). In these studies, positive δ^{56}Fe in Fe oxides and carbonates are interpreted as inheritance from a ferric oxyhydroxide precursor formed in the upper water column by partial Fe(II) oxidation. In this case, only part of the reservoir of dissolved Fe(II) was oxidized as the oxidant was the limiting factor. Carbonates with δ^{56}Fe values of ~−0.5‰ are suggested to have formed in equilibrium with seawater ($\delta^{56}Fe/‰ = [(^{56/54}Fe_{Sample}/^{56/54}Fe_{IRMM\text{-}014}) - 1] * 1000$). In contrast, magnetite and carbonates with strong negative δ^{56}Fe values are attributed to the activity of microbial dissimilatory iron reduction (DIR) during diagenesis, which seems to have played an important role in the formation of BIFs. Silicon isotope variations in chert have been investigated in few BIF samples, so far giving a range from −2.6‰ to −0.5‰ in δ^{30}Si ($\delta^{30}Si/‰ = [(^{30/28}Si_{Sample}/^{30/29}Si_{NBS28}) - 1] * 1000$) (Jiang et al., 1993; Ding et al., 1996; André et al., 2006; Steinhoefel et al., 2009a). The general consensus is that light Si isotopes preferentially precipitate from solution (De La Rocha et al., 1997; Ziegler et al., 2005; Basile-Doelsch, 2006), although it still lacks experimental verification. Precambrian chert deposits appear to record the original isotope signature because small-scale Si isotope variations are preserved (André et al., 2006; van den Boorn et al., 2007, 2010; Steinhoefel et al., 2009a). Negative δ^{30}Si values are considered to reflect a hydrothermal signature (Jiang et al., 1993; Ding et al., 1996; André et al., 2006; Steinhoefel et al., 2009a; van den Boorn et al., 2010). In contrast, positive δ^{30}Si values may reflect elevated temperature of the seawater, the influence of a continental source or precipitation from isotopically heavy seawater (Robert and Chaussidon, 2006; van den Boorn et al., 2007, 2010).

In this study, we present high-spatial resolution Fe and Si isotope data on BIFs of the Transvaal and Hamersley successions determined by femtosecond laser ablation coupled to a multicollector inductively coupled plasma mass spectrometer (MC-ICP-MS). This analytical development allows us to investigate the relative differences of the isotope composition of coexisting mineral phases in distinct BIF layers, an ability that presents a significant advantage in exploring the genetic processes of BIF formation together with temporal changes of these processes as BIFs are deposited.

2. INVESTIGATED BIF SAMPLES

2.1. Geological background

The most laterally extensive and best preserved BIFs were deposited within the Transvaal Supergroup, South Africa and the Hamersley Group, Australia (for a recent review see Beukes and Gutzmer (2008)). They represent typical Proterozoic iron formations formed within continental shelf areas. Most of these BIFs have experienced only low-grade metamorphism, which makes them ideally suited for this study. The iron formations exhibit a broad spectrum of textural and mineralogical rock types (e.g. Beukes and Gutzmer, 2008). They range from clastic-textured allochemical to orthochemical microbanded micritic iron formations, which were deposited from high energy environments within shallow-shelf areas to deep water basins. Depending on the major Fe-bearing mineral phases, they are classified as oxide, carbonate and silicate facies with several mixed facies.

The Transvaal Supergroup is mainly preserved within the Transvaal and the correlated Griqualand West Basin in South Africa on the Archean Kaapvaal Craton. The northeastern part is thought to be deposited within small basins that widened to the south-west towards the open ocean (Bau and Dulski, 1992). The Transvaal BIFs represent shelf deposits in a partly enclosed basin, with depositional environments ranging from deep- to very shallow-water settings (Klein and Beukes, 1989; Beukes and Gutzmer, 2008). Our samples have been taken from the Kuruman Iron Formation in the Griqualand West Basin and from the correlated Penge Iron Formation in the Transvaal Basin. The Kuruman Iron Formation contains alternating siderite–chert–magnetite microbanded macrocycles (Beukes, 1980) and experienced very low-grade metamorphism with temperatures between 110 and 170 °C (Miyano and Beukes, 1984). The Penge Iron Formation was locally affected by contact metamorphism of up to 500 °C caused by the 2.06 Ga Bushveld intrusion (Sharpe and Chadwick, 1982; Walraven et al., 1990). Hydrothermal orebodies were formed by hydrothermal oxidative fluids, a late event related to the Bushveld intrusion, and were further modified by Late Mesozoic deep lateritic weathering (Gutzmer et al., 2005). SHRIMP U–Pb zircon ages of stilpnomelane-rich tuffaceous mudstones yield an upper age of 2.46 Ga for the Kuruman Iron Formation (Pickard, 2003).

The sediments within the Hamersley Basin were deposited on the Archean Pilbara Craton in Western Australia. The Hamersley succession is considered to be formed on a semi-isolated marine platform within a back-arc basin (Blake and Barley, 1992; Morris, 1993). The investigated sample material was taken from the 160 m thick Dales Gorge Member. It is the lowermost unit of the Brockman Iron Formation of the Hamersley Group, which is part of the Mount Bruce Supergroup. The Dales Gorge Member comprises 33 Fe oxide-rich and carbonate-silicate-rich "macrobands" alternating in a scale of decimeter to meter (Trendall and Blockley, 1970). U–Pb SHRIMP data of zircons from intercalated tuffaceous layers reveal a depositional age between 2.49 and 2.46 Ga for the whole member (Trendall et al., 2004). The unit experienced very low-grade metamorphism with temperatures between 60 and 160 °C at the Paraburdoo area, from which the sample material originated (Ewers and Morris, 1981; Kaufman et al., 1990).

The similar depositional ages indicate that the Kuruman Iron Formation and the Brockman Iron Formation were deposited synchronously (Pickard, 2003). Sedimentation rates of consolidated material are in the range of about 33 m per 10^6 year for both BIFs based on SHRIMP U–Pb ages (Pickard, 2002, 2003). REE patterns with positive Eu anomalies and mantle-like Nd isotope signatures of the BIFs reveal a strong influence of a hydrothermal component in the seawater (Klein and Beukes, 1989; Bau and Dulski, 1992, 1996; Alibert and McCulloch, 1993; Morris, 1993; Bau et al., 1997). Conversely, Ge/Si data from the Dales Gorge Member within the Brockman Iron Formation suggest a significant contribution of Si sourced from continental weathering (Hamade et al., 2003). Similarities in age and stratigraphy between the Transvaal and the Hamersley successions (see overview in Beukes and Gutzmer (2008)) give rise to speculations whether these iron formations have been deposited on the same continent within a single partly enclosed ocean basin (e.g. Cheney, 1996; Beukes and Gutzmer, 2008) and might have been the response to widespread magmatic events (e.g. Isley and Abbott, 1999; Nelson et al., 1999).

2.2. Sample description

We have investigated four core sections from BIFs with a length of 3.5 to 5 cm. Three samples (3/79, 3/59 and DGM-36) are from pristine orthochemical mircobanded micritic iron formations belonging to the oxide to carbonate facies and were deposited in similar environments. The chemical composition of the various mineral phases in the investigated BIF samples was examined by electron microprobe. Fe oxides exhibit very pure stoichiometric compositions; the variability in Fe carbonate composition is presented in Table 1.

The core sections, 3/79 and 3/59, are from the Kuruman Iron Formation sampled from the core DW-19A, which was drilled at Pomfret in the north of the Griqualand West Basin. Sample 3/79 represents a magnetite–hematite–chert BIF consisting of alternating Fe oxide- and chert-rich layers on a centimeter to millimeter scale. Magnetite is the major Fe oxide phase, which is partly intergrown with hematite. Both minerals occur as anhedral aggregates. Chert layers are pigmented by fine hematite dust. Core section 3/59 represents a typical laminated magnetite–carbonate–chert BIF (Fig. 1c). Magnetite crystals are sub- to euhedral of about 30 μm in size. Carbonate phases comprising calcite, siderite and ankerite form either distinct compact layers or occur as finely distributed aggregates. The Fe-bearing varieties are ankerite, $Ca(Fe_{0.30–0.60}, Mg_{0.40–0.70})(CO_3)_2$, and siderite with variable Mg-substitution, $(Fe_{0.70–0.80}, Mg_{0.20–0.30})CO_3$ and $(Fe_{0.55}, Mg_{0.45})CO_3$. The chemical composition of the investigated layers is presented in Table 1 and depicted in Fig. 2. Chert is occasionally red pigmented by hematite dust. The lamination is defined by variable proportions of the constituent minerals.

Table 1
Average chemical composition (in wt.% ±2 SD) determined by electron microprobe and mean Fe isotope composition of Fe carbonate phases.

mm	Mineral	FeO	MnO	MgO	CaO	*n*	$\delta^{56}Fe_{mean}$
Kuruman Iron Formation 3/59 (Transvaal)							
38.70	ank	18.71 ± 1.06	1.33 ± 0.18	7.98 ± 0.60	27.43 ± 1.06	7	−0.72
	Mg-sid	39.79 ± 2.22	1.20 ± 0.44	17.48 ± 2.10	0.38 ± 0.34	19	−0.88
	sid	50.77 ± 3.54	1.97 ± 0.74	6.99 ± 3.74	0.48 ± 0.42	9	−0.72
38.55	ank	16.95 ± 6.66	1.02 ± 0.64	9.49 ± 6.98	27.92 ± 1.00	11	−0.66
	Mg-sid	39.79 ± 0.60	1.13 ± 0.20	18.09 ± 0.14	0.33 ± 0.36	3	−0.90
37.75	ank	17.86 ± 3.92	1.21 ± 0.38	8.04 ± 4.56	27.95 ± 0.64	6	−0.84
20.80	ank	19.16 ± 2.40	1.26 ± 0.48	8.27 ± 1.52	26.51 ± 0.80	19	−0.89
	sid	51.98 ± 3.94	1.72 ± 0.70	6.50 ± 2.94	0.49 ± 0.34	20	−0.65
3.65	sid	52.32 ± 2.93	1.65 ± 0.79	5.84 ± 1.91	0.51 ± 0.35	8	−0.83
3.45	sid	52.40 ± 2.55	1.64 ± 0.64	5.84 ± 1.47	0.44 ± 0.36	3	−0.69
3.00	sid	52.19 ± 2.98	1.65 ± 0.68	5.85 ± 2.00	0.46 ± 0.78	5	−0.75
0	Mg-sid	45.10 ± 1.50	2.03 ± 0.12	11.74 ± 0.46	0.58 ± 0.24	2	−1.13
	ank	17.71 ± 4.64	1.48 ± 0.32	8.96 ± 3.64	27.19 ± 0.56	3	−1.20
Dales Gorge Member DGM-36 (Hamersley)							
35.82	sid	43.07 ± 9.19	0.64 ± 0.75	13.56 ± 9.33	1.26 ± 1.621	6	−2.18
24.84	sid (rim)	49.08 ± 2.40	0.74 ± 0.26	9.65 ± 1.58	0.34 ± 0.28 16	16	
	sid (core)	51.99 ± 1.34	0.89 ± 0.30	6.77 ± 2.69	0.77 ± 1.17	4	−1.97

The stratigraphic position of each investigated Fe carbonate phase (sid = siderite, Mg-sid = siderite with significant Mg-substitution and ank = ankerite) is indicated by mm corresponding to Fig. 3. Complete Fe isotope datasets are provided in Table 2. As visible in Fig. 1a, sample DGM-36 exhibits siderite rhombs with two growth stages indicated by 'sid (rim)' and 'sid (core)'.

Core sample DGM-36 represents BIF macroband 16 of the Dales Gorge Member of the Brockman Iron Formation. It originated from drillhole DDH-44 at Paraburdoo sited at the south-west edge of the Hamersley Basin. The sample is a finely laminated hematite–magnetite–siderite–chert BIF. Iron-rich layers consist mainly of hematite, magnetite and minor siderite. Hematite is texturally variable displaying massive, anhedral to fine platy habits. Subhedral magnetite typically occurs as overgrowths on hematite laminae (Fig. 1b). Siderite, $(Fe_{0.75}, Mg_{0.25})CO_3$, appears as very finely distributed phase or in the form of subhedral rhomboids with distinct growth zones (Fig. 1a). Chert is interbedded with Fe-rich layers. Detailed petrographic and geochemical information on this sample are given by Pecoits et al. (2009). Sample TBT represents a BIF altered by iron ore mineralization. It originates from the Penge Iron Formation and was collected in the mining area around Thabazimbi in the northern Transvaal Basin. It consists of alternating micro-layers of hematite and chert, as well as layers of massive chert, which are pigmented by very fine hematite dust. Hydrothermal ore formation in the Thabazimbi area is related to a hydrothermal fluid infiltration event, which caused oxidative carbonate metasomatism (Gutzmer et al., 2005; De Kock et al., 2008). As a consequence, hematite replaced magnetite, grunerite and Fe carbonates. This hematite-chert BIF sample might represent a former magnetite-chert BIF as relict minerals other than magnetite are absent. The sample is almost completely oxidized as all chert layers appear red and evidence for incomplete martitization processes (transformation of magnetite into hematite by oxidation of magnetite, e.g. Mücke, 2003) is very rare. Evidence of supergene modifications such as leaching of chert is absent.

3. METHODS

High-spatial resolution Fe and Si isotope data of the investigated BIFs were obtained *in situ* from thin sections by laser ablation MC-ICP-MS (LA-MC-ICP-MS) at the Leibniz University of Hannover. The instrumental setup consists of our in-house built UV femtosecond laser ablation system coupled to a ThermoFinnigan Neptune MC-ICP-MS and has been described in detail by Horn and von Blanckenburg (2007). The analytical method followed the procedure of Horn et al. (2006), Chmeleff et al. (2008) and Steinhoefel et al. (2009a). The instrumental mass discrimination was corrected by standard-sample-bracketing using the reference materials IRMM-014 and NBS28 for Fe and Si isotope analysis, respectively. The external reproducibilities for both raster and spot analyses of homogeneous materials are ~0.1‰ (2 SD) and ~0.2‰ (2 SD) on $\delta^{56}Fe$ and $\delta^{57}Fe$, respectively, and have been verified for different types of matrices including those investigated herein (Horn et al., 2006; Steinhoefel et al., 2009a,b). The Fe isotope data are reported as $\delta^{56}Fe$ and $\delta^{57}Fe$ relative to the reference material IRMM-014

$$\frac{\delta^{56}Fe}{‰} = \left(\frac{^{56}Fe/^{54}Fe_{Sample}}{^{56}Fe/^{54}Fe_{IRMM\text{-}014}} - 1\right) * 1000 \quad (1)$$

$$\frac{\delta^{57}Fe}{‰} = \left(\frac{^{57}Fe/^{54}Fe_{Sample}}{^{57}Fe/^{54}Fe_{IRMM\text{-}014}} - 1\right) * 1000 \quad (2)$$

Analyses of Si isotopes reveal an overall precision for $\delta^{29}Si$ and $\delta^{30}Si$ of 0.15‰ (2 SD) and 0.24‰ (2 SD), respectively (Chmeleff et al., 2008). The Si isotope data are presented as $\delta^{29}Si$ and $\delta^{30}Si$ relative to the reference material NBS28

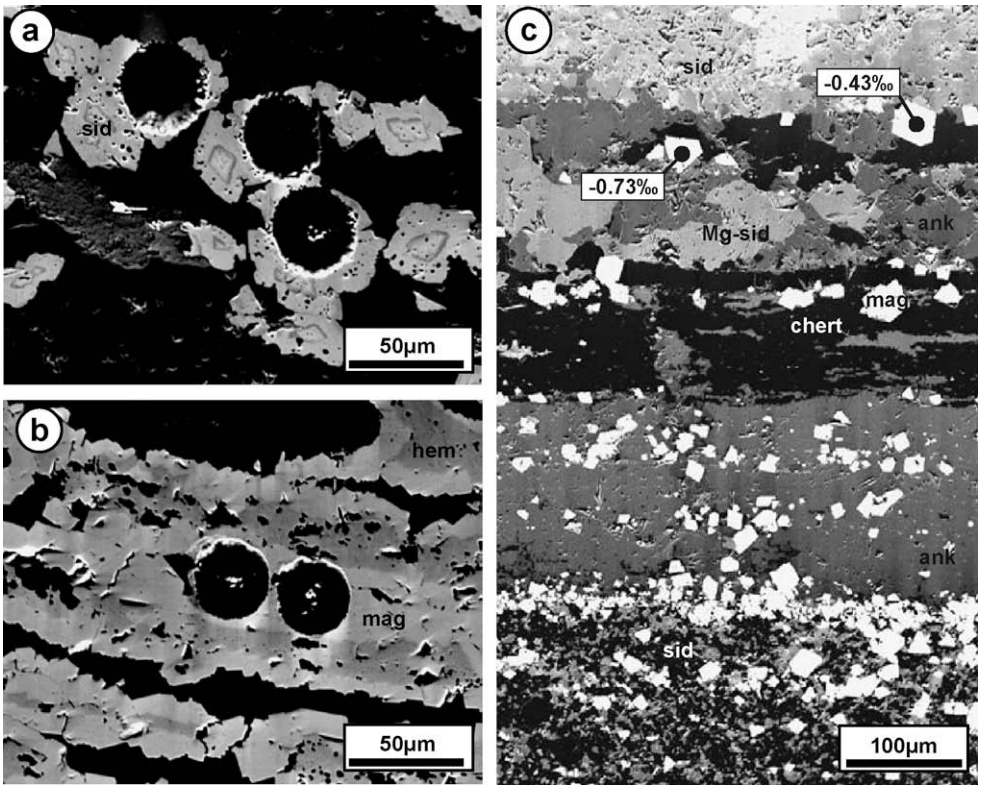

Fig. 1. Backscattered electron (BSE) images of BIF samples with sid = siderite, Mg-sid = Mg-rich siderite, ank = ankerite, mag = magnetite, hem = hematite and chert = quartz. (a and b) The images show laser ablation craters in siderite rhomboids and magnetite, respectively, in sample DGM-36. (c) Carbonate–magnetite–chert layers in sample 3/59. Magnetite exposes abrupt shifts of δ^{56}Fe within few microns as observable between 38.70 and 38.55 mm of the core section.

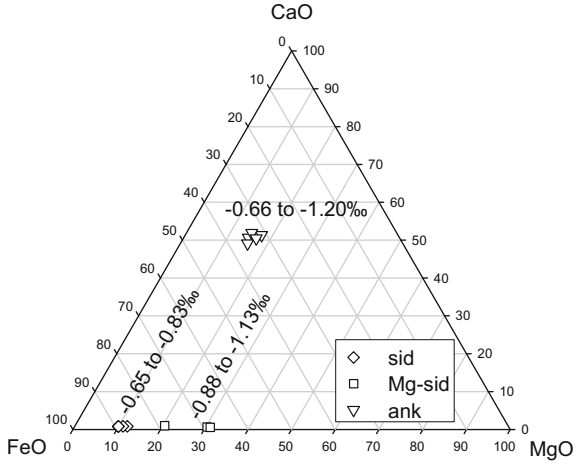

Fig. 2. Carbonate composition, as mole percent of CaO, MgO and FeO and observed ranges in mean δ^{56}Fe values of sample 3/59. The data are listed in Tables 1 and 2. The Fe carbonate phases, sid = siderite, Mg-sid = Mg-rich siderite and ank = ankerite each show uniform chemical compositions but differ in the range of their Fe isotope composition. Siderite exhibits a small range in δ^{56}Fe, whereas siderite with significant Mg-substitution and ankerite are depleted in heavy Fe relative to siderite to a range of degrees.

$$\frac{\delta^{30}\mathrm{Si}}{‰} = \left(\frac{^{30}\mathrm{Si}/^{28}\mathrm{Si}_{\mathrm{Sample}}}{^{30}\mathrm{Si}/^{28}\mathrm{Si}_{\mathrm{NBS28}}} - 1\right) * 1000 \quad (3)$$

$$\frac{\delta^{29}\mathrm{Si}}{‰} = \left(\frac{^{29}\mathrm{Si}/^{28}\mathrm{Si}_{\mathrm{Sample}}}{^{29}\mathrm{Si}/^{28}\mathrm{Si}_{\mathrm{NBS28}}} - 1\right) * 1000 \quad (4)$$

We investigated the Fe isotope compositions of all major Fe-bearing mineral phases in selected layers of the sampled BIFs. Iron oxides were analysed by spot analysis with a diameter of 20–30 μm. Single magnetite crystals in sample 3/59 were investigated by the experimental procedure described in Steinhoefel et al. (2009a) to examine potential intra-mineral isotope zonation. Sequential coring by laser ablation using different spot sizes allows to analyse the Fe isotope composition of the crystal core and the rim, separately, in crystals as large as 30 μm. Iron carbonates were investigated prior to Fe isotope analysis by electron microprobe to distinguish distinct phases. Backscattered electron (BSE) images assisted to analyse pure phases using short line scans. Multiple analyses were performed parallel and perpendicular to the lamination to investigate the variability of the Fe isotope composition of the different mineral phases.

The Si isotope composition was investigated in chert. Analyses using narrow rasters of about 50 μm × 500 μm provide a high-spatial resolution in chert layers.

In addition to Fe and Si isotope ratios, we investigated the C isotope composition in sample 3/59, in which Fe

carbonates represent one of the major mineral phases. Micro-sampling of individual layers was performed on a thick section using a 0.5 mm diameter steel drill bit tipped with synthetic diamonds. The analyses were carried out at the Leibniz Institute for Applied Geophysics in Hannover using a fully automated preparation system (ThermoFinnigan Gasbench 2) directly coupled to a ThermoFinnigan Delta Plus XP isotope ratio mass spectrometer following a standard procedure (e.g. Spotl and Vennemann, 2003). All samples were measured in duplicate and reported as mean $\delta^{13}C$ value relative to the PDB standard. The external reproducibility is better than 0.2‰ (2 SD).

4. RESULTS

4.1. Fe isotope composition

The Fe isotope compositions of the various Fe-bearing mineral phases in the investigated BIF samples are presented in Fig. 3 and in Table 2. The chemical composition of Fe carbonate phases and their corresponding mean $\delta^{56}Fe$ values are summarized in Table 1 and depicted in Fig. 2. Hematite micro-layers of sample TBT exhibit significant lateral variation in their $\delta^{56}Fe$ values on a sub-millimeter scale (Fig. 3a). This variation exceeds the analytical uncertainties. Average Fe isotope compositions among micro-layers however remain uniform (Fig. 3b). The maximal observed lateral range is −1.17‰ to 0.27‰ in $\delta^{56}Fe$ with an average of -0.47 ± 0.52‰ (2 SD, $n = 14$) at 11.15 mm of the investigated section. Similar variations have been found within other layers with ±0.11‰ to 0.44‰ (2 SD, $n = 8$–16). A comparison of the mean $\delta^{56}Fe$ values of the boundaries of micro-layers reveals no significant differences in most cases (Student's *t*-test, 95% confidence level); also inter-layer trends in the Fe isotope composition are absent (Fig. 3b). The data can be considered as Gaussian distribution with a mean of -0.39 ± 0.31‰ (2 SD, $n = 181$). This observation may reflect one dominating process, which has caused the small-scale variation in the Fe isotope composition.

In sample 3/79, magnetite and hematite show homogeneous Fe isotope compositions within individual layers, although differences from layer to layer do exist (Fig. 3d and e). Hematite reveals little variations in $\delta^{56}Fe$ giving mean values between −0.17‰ and −0.02‰ for different stratigraphic levels, while magnetite is more variable with mean $\delta^{56}Fe$ values ranging between −0.59‰ and −0.14‰. Magnetite shows consistently lower $\delta^{56}Fe$ values than hematite with relative difference between them ranging between 0.08‰ and 0.50‰.

In sample 3/59, magnetite and the Fe carbonate phases (siderite, Mg-rich siderite and ankerite) were investigated (Figs. 2, 3g, h and 4). Repeated analyses reveal that all mineral phases are homogeneous in their Fe isotope composition within individual laminations. Magnetite exhibits significant variations in $\delta^{56}Fe$ perpendicular to the lamination with abrupt shifts within a few microns giving mean values between −0.86‰ and −0.02‰ (Figs. 1c and 3h). The examination of individual magnetite grains at 39.20 mm of the investigated core section reveals isotopically homogeneous crystals within the analytical precision giving mean $\delta^{56}Fe$ values of -0.48 ± 0.11‰ (2 SD, $n = 18$) for the crystal core and -0.44 ± 0.25‰ (2 SD, $n = 12$) for the crystal rim (Fig. 4). The Fe isotope composition of Fe carbonate phases shows no direct correlation with chemical composition (Table 1 and Fig. 2). Mean $\delta^{56}Fe$ values for siderite are relatively constant ranging between −0.83‰ and −0.65‰, whereas siderite with significant Mg-substitution is slightly more variable with $\delta^{56}Fe$ values between −1.13‰ and −0.88‰. Ankerite is the most variable phase giving mean $\delta^{56}Fe$ values between −1.20‰ and −0.66‰. Increased standard deviations of multiple Fe isotope analyses of individual Fe carbonate phases are attributed to slightly variable chemical compositions.

In the sample DGM-36, hematite and magnetite show little inter-layer variations with mean $\delta^{56}Fe$ values ranging from −0.90‰ to −0.76‰ and from −0.94‰ to −0.82‰, respectively (Fig. 3j–k). Variations of ±0.13‰ to 0.41‰ (2 SD, $n = 6$–19) for multiple analyses partly differ significantly from the analytical precision indicating heterogeneous Fe isotope compositions within individual layers. Coexisting hematite and magnetite have identical Fe isotope compositions within the analytical precision. Very fine distributed siderite occurring adjacent to magnetite and hematite could be analysed only once giving a $\delta^{56}Fe$ value of −2.18‰. Siderite rhombs within a hematite–siderite-rich layer reveal a mean $\delta^{56}Fe$ value of −1.97‰.

4.2. Si isotope composition

The Si isotope data of chert in the investigated BIFs are presented in Table 4 and are depicted in Fig. 3. Silicon isotope compositions of chert in all investigated samples are homogeneous, but distinctly light. Samples from the Transvaal succession TBT, 3/59 and 3/79 exhibit mean $\delta^{30}Si$ value of -0.82 ± 0.22‰ (2 SD, $n = 31$), -1.22 ± 0.31‰ (2 SD, $n = 27$) and -0.77 ± 0.26‰ (2 SD, $n = 31$), respectively. DGM-36 from the Hamersley succession is slightly more variable giving a mean $\delta^{30}Si$ value of -1.25 ± 0.40‰ (2 SD, $n = 36$).

4.3. C isotope composition

The C isotope composition was investigated in carbonate-rich layers in sample 3/59. $\delta^{13}C$ values of bulk layers range between −10.91‰ and −8.95‰ giving a mean value of -9.85 ± 1.26‰ (2 SD, $n = 9$) (Table 3 and Fig. 5).

5. DISCUSSION

5.1. Formation of mineral phases in BIFs investigated

5.1.1. Formation of chert

Chert in BIFs is considered to be an early diagenetic phase derived either from a silica gel or siliceous ferric oxyhydroxide precursor. Silica precipitation might have occurred directly from seawater saturated by Si or was promoted by absorption of Si on Fe hydroxides (e.g. Perry and Lefticariu, 2003; Maliva et al., 2005; Konhauser et al., 2007a; Fischer and Knoll, 2009). It is assumed that early

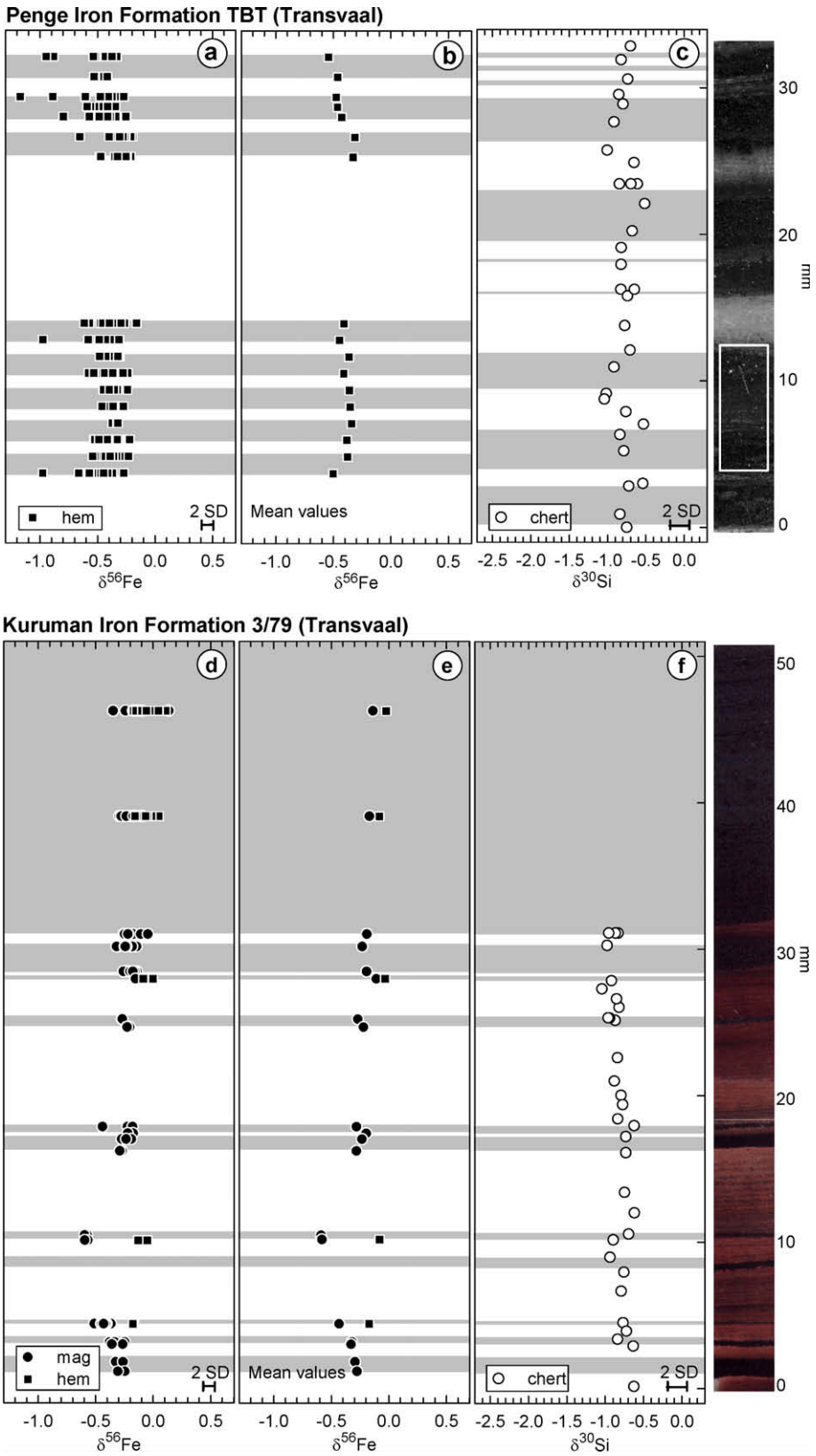

Fig. 3. Iron and silicon isotope variations in the Penge and Kuruman Iron Formation from the Transvaal succession and in the Dales Gorge Member of the Brockman Iron Formation from the Hamersley succession. Mineral phases are presented by hem = hematite, mag = magnetite, sid = siderite, Mg-sid = Mg-rich siderite, ank = ankerite and chert = quartz. (a, d, g and j) All obtained Fe isotope data, whereas (b, e, h and k) present mean δ^{56}Fe values of multiple analyses. Iron isotope data on sample TBT were obtained from the marked section. (c, f, i and l) δ^{30}Si values of single raster analyses. The investigated core sections represent about 1000–1500 years of deposition assuming a deposition rate of 0.033 mm/year (Pickard, 2002, 2003).

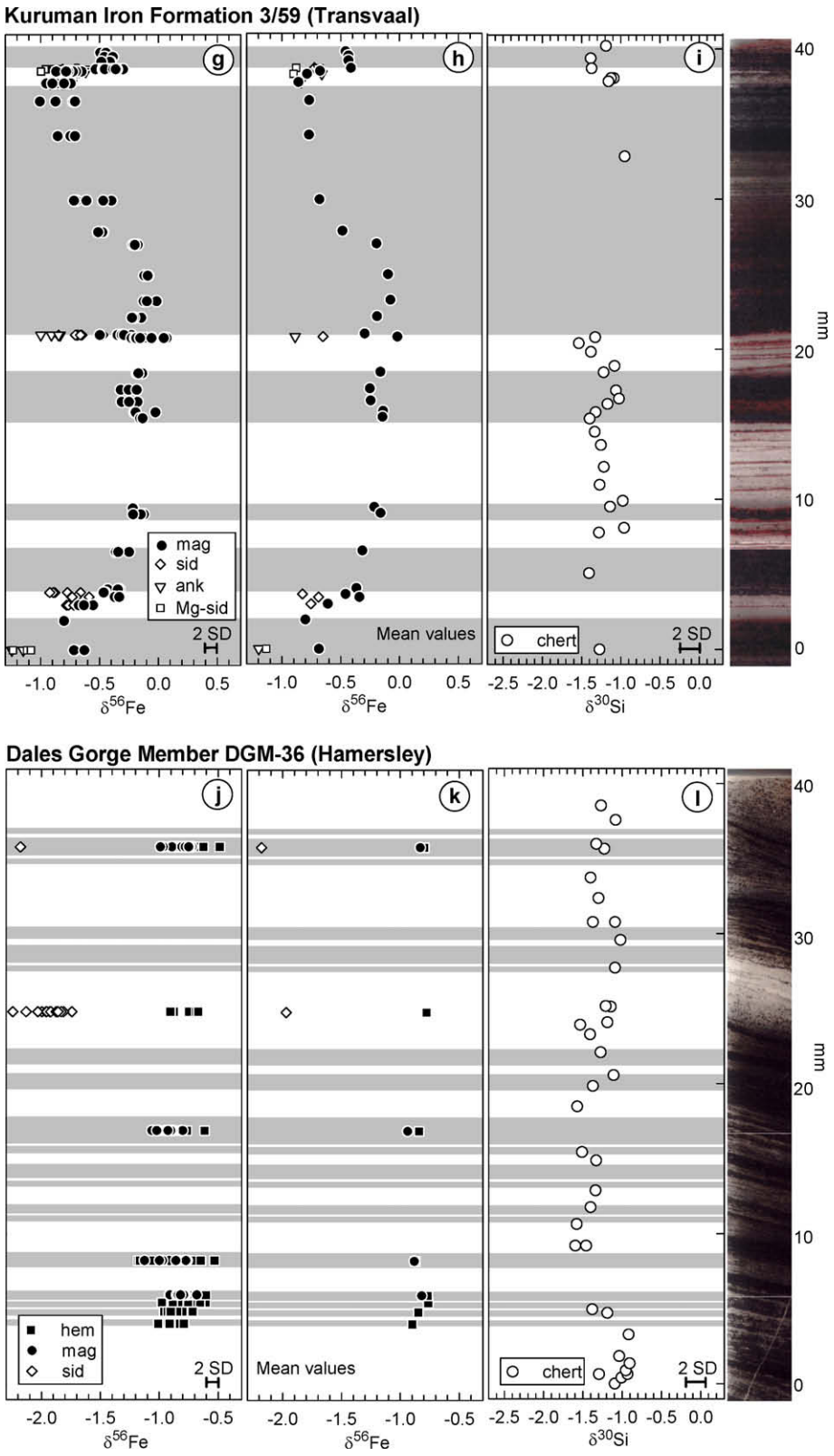

Fig. 3 (*continued*)

diagenetic chert reflects the processes of the initial Si deposition (e.g. Knauth, 1994; Maliva et al., 2005). This assumption is also supported by small-scale Si isotope variations exposed in Precambrian chert deposits (André et al.,

Table 2
Fe isotope data of investigated BIFs obtained by LA-MC-ICP-MS.

mm	Mineral	$\delta^{56}Fe_{mean}$	$\delta^{57}Fe_{mean}$	*n*
Dales Gorge Member DGM-36 (Hamersley)				
35.82	mag	−0.83 ± 0.16	−1.18 ± 0.19	19
	hem	−0.80 ± 0.29	−1.09 ± 0.34	11
	sid	−2.18	−3.02	1
24.84	hem	−0.78 ± 0.22	−1.05 ± 0.30	5
	sid	−1.97 ± 0.34	−2.74 ± 0.49	15
16.92	mag	−0.94 ± 0.15	−1.31 ± 0.13	15
	hem	−0.84 ± 0.19	−1.18 ± 0.28	16
8.26	mag	−0.88 ± 0.24	−1.23 ± 0.29	10
	hem	−0.87 ± 0.41	−1.21 ± 0.47	12
5.96	mag	−0.82 ± 0.13	−1.20 ± 0.14	13
	hem	−0.77 ± 0.15	−1.13 ± 0.23	18
5.46	hem	−0.76 ± 0.20	−1.05 ± 0.30	16
4.86	hem	−0.85 ± 0.16	−1.17 ± 0.24	11
4.06	hem	−0.90 ± 0.14	−1.25 ± 0.28	6
Kuruman Iron Formation 3/59 (Transvaal)				
39.80	mag	−0.46 ± 0.06	−0.68 ± 0.08	3
39.52	mag	−0.43 ± 0.08	−0.64 ± 0.11	3
39.20	mag	−0.43 ± 0.09	−0.63 ± 0.13	3
38.70	mag	−0.41 ± 0.13	−0.61 ± 0.15	19
	ank	−0.72 ± 0.14	−1.06 ± 0.23	5
	Mg-sid	−0.88 ± 0.12	−1.28 ± 0.20	12
	sid	−0.72 ± 0.12	−1.03 ± 0.25	4
38.55	mag	−0.75 ± 0.14	−1.09 ± 0.25	8
	ank	−0.66 ± 0.08	−0.95 ± 0.04	3
	Mg-sid	−0.90 ± 0.16	−1.32 ± 0.23	3
37.75	mag	−0.86 ± 0.14	−1.28 ± 0.24	7
	ank	−0.84 ± 0.14	−1.19 ± 0.25	6
36.55	mag	−0.77 ± 0.18	−1.11 ± 0.36	4
34.25	mag	−0.77 ± 0.15	−1.17 ± 0.22	3
29.95	mag	−0.68 ± 0.10	−0.99 ± 0.16	6
26.75	mag	−0.49 ± 0.04	−0.75 ± 0.12	3
25.95	mag	−0.20 ± 0.04	−0.27 ± 0.13	3
23.85	mag	−0.10 ± 0.04	−0.14 ± 0.09	3
22.15	mag	−0.08 ± 0.11	−0.09 ± 0.19	3
20.95	mag	−0.19 ± 0.08	−0.25 ± 0.07	3
19.85	mag	−0.30 ± 0.09	−0.45 ± 0.18	6
19.65	mag	−0.02 ± 0.15	−0.03 ± 0.13	14
	ank	−0.89 ± 0.14	−1.26 ± 0.15	5
	sid	−0.65 ± 0.24	−0.92 ± 0.28	8
17.45	mag	−0.16 ± 0.05	−0.21 ± 0.07	3
16.35	mag	−0.25 ± 0.14	−0.36 ± 0.21	3
15.55	mag	−0.25 ± 0.13	−0.34 ± 0.17	4
14.85	mag	−0.14 ± 0.20	−0.18 ± 0.23	4
14.45	mag	−0.15 ± 0.02	−0.19 ± 0.06	4
9.45	mag	−0.21 ± 0.01	−0.33 ± 0.04	2
9.05	mag	−0.16 ± 0.10	−0.20 ± 0.12	3
7.05	mag	−0.32 ± 0.12	−0.49 ± 0.17	3
4.05	mag	−0.37 ± 0.11	−0.50 ± 0.22	3
3.85	mag	−0.46 ± 0.02	−0.60 ± 0.34	2
	sid	−0.83 ± 0.22	−1.16 ± 0.21	5
3.55	mag	−0.34 ± 0.05	−0.41 ± 0.16	3
	sid	−0.69 ± 0.14	−1.00 ± 0.17	4
3.00	mag	−0.61 ± 0.11	−0.85 ± 0.22	4
	sid	−0.75 ± 0.06	−1.09 ± 0.41	3
1.95	mag	−0.80	−1.13	1
0.00	mag	−0.69 ± 0.10	−1.00 ± 0.17	3
	Mg-sid	−1.13 ± 0.14	−1.68 ± 0.14	4
	ank	−1.20 ± 0.14	−1.66 ± 0.06	2
Kuruman Iron Formation 3/79 (Transvaal)				
46.25	mag	−0.14 ± 0.20	−0.19 ± 0.26	15
	hem	−0.02 ± 0.17	−0.03 ± 0.21	14
39.05	mag	−0.17 ± 0.14	−0.25 ± 0.20	12
	hem	−0.08 ± 0.12	−0.11 ± 0.22	14
31.00	mag	−0.19 ± 0.14	−0.25 ± 0.21	9
30.15	mag	−0.23 ± 0.11	−0.31 ± 0.20	9
28.45	mag	−0.19 ± 0.07	−0.27 ± 0.17	9
27.95	mag	−0.11 ± 0.08	−0.16 ± 0.12	3
	hem	−0.03 ± 0.09	−0.01 ± 0.15	3
25.20	mag	−0.27 ± 0.01	−0.35 ± 0.04	2
24.65	mag	−0.22 ± 0.03	−0.31 ± 0.05	3
17.85	mag	−0.28 ± 0.28	−0.45 ± 0.41	3
17.40	mag	−0.20 ± 0.07	−0.25 ± 0.17	2
17.00	mag	−0.23 ± 0.08	−0.33 ± 0.17	3
16.20	mag	−0.28 ± 0.02	−0.39 ± 0.08	3
10.45	mag	−0.59 ± 0.02	−0.87 ± 0.05	3
10.10	mag	−0.58 ± 0.04	−0.85 ± 0.10	2
	hem	−0.08 ± 0.08	−0.12 ± 0.16	3
4.40	mag	−0.43 ± 0.09	−0.64 ± 0.12	7
4.40	hem	−0.17 ± 0.01	−0.30 ± 0.11	2
4.15	mag	−0.32 ± 0.13	−0.48 ± 0.11	3
3.00	mag	−0.33 ± 0.11	−0.43 ± 0.15	3
1.80	mag	−0.29 ± 0.09	−0.38 ± 0.08	2
1.15	mag	−0.28 ± 0.09	−0.37 ± 0.13	2
Penge Iron Formation TBT (Transvaal)				
11.90	hem	−0.54 ± 0.44	−0.63 ± 0.96	9
11.55	hem	−0.46 ± 0.12	−0.62 ± 0.83	3
11.15	hem	−0.47 ± 0.52	−0.60 ± 0.89	14
10.95	hem	−0.46 ± 0.15	−0.59 ± 0.29	8
10.75	hem	−0.43 ± 0.29	−0.59 ± 0.41	14
10.48	hem	−0.31 ± 0.23	−0.40 ± 0.47	13
10.05	hem	−0.33 ± 0.19	−0.42 ± 0.23	9
6.90	hem	−0.41 ± 0.22	−0.51 ± 0.52	16
6.55	hem	−0.45 ± 0.32	−0.60 ± 0.46	15
6.28	hem	−0.36 ± 0.11	−0.45 ± 0.42	10
5.90	hem	−0.41 ± 0.23	−0.54 ± 0.29	8
5.65	hem	−0.36 ± 0.13	−0.47 ± 0.41	9
5.25	hem	−0.36 ± 0.11	−0.53 ± 0.22	9
5.05	hem	−0.34 ± 0.05	−0.44 ± 0.47	3
4.65	hem	−0.38 ± 0.26	−0.45 ± 0.55	9
4.40	hem	−0.37 ± 0.18	−0.53 ± 0.24	16
4.00	hem	−0.50 ± 0.33	−0.71 ± 0.42	16

The stratigraphic positions of the analysed mineral phases (mag = magnetite, hem = hematite, sid = siderite, Mg-sid = siderite with significant Mg-substitution and ank = ankerite) are indicated by mm corresponding to Fig. 3. Uncertainties given by 2 standard deviations refer to multiple analyses (*n*).

2006; van den Boorn et al., 2007; Steinhoefel et al., 2009a). Hence, we also assume preservation of initial isotope signatures in the pristine BIF samples investigated here. Also, no evidence is apparent to suggest post-depositional Si redistribution. Therefore, the uniform Si isotope signatures of the investigated core sections suggest continuous silica precipitation from well-mixed seawater with a steady Si isotope composition. Silicon isotope fractionation occurring at silica gel precipitation from solution is not well constrained,

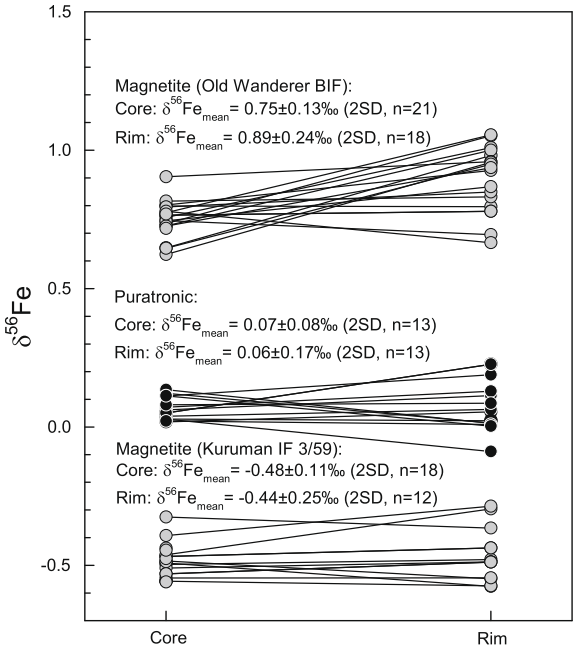

Fig. 4. Investigation of intra-crystal Fe isotope heterogeneity in magnetite using a method described in Steinhoefel et al. (2009a). Magnetite crystals in the Archean Old Wanderer BIF from the Shurugwi Greenstone Belt (Zimbabwe) show zonation in the Fe isotope composition revealed by corresponding pairs of core-rim analysis (Steinhoefel et al., 2009a), whereas magnetite in sample 3/59 from the Kuruman Iron Formation exhibits homogeneous crystals. The analytical procedure has been validated on the homogeneous metal standard Puratronic showing that the inner spot analyses (=core) are identical with the outer spot analyses (=rim) within the analytical precision (Steinhoefel et al., 2009a).

but estimates for the difference between fluid and precipitate are in the order of −1.5‰ (De La Rocha et al., 1997; Ziegler et al., 2005; Basile-Doelsch, 2006). Adsorption of Si onto iron oxides produces isotope fractionation that is within the same range (Delstanche et al., 2009). Taking this fractionation factor together with the Si isotope composition of the investigated samples 3/59 3/79 and DGM-36 with mean δ^{30}Si values of −1.22‰, −0.77‰ and −1.25‰, respectively, silica originated from seawater with a Si isotope signature ranging between 0.2‰ and 0.7‰.

Table 3
C isotope data of bulk layers of sample 3/59 from the Kuruman Iron Formation (Transvaal).

mm	Carbonate composition of layers	δ^{13}C
38.35	50% sid, 50% ank	−9.51
34.25	95% calcite, 5% sid	−9.57
29.95	95% calcite, 5% sid	−9.58
27.85	95% calcite, 5% sid	−9.59
20.55	80% ank, 20% sid	−10.29
11.00	60% ank, 40% sid	−10.12
3.45	20% ank, 80% sid	−11.17
1.50	70% ank, 30% sid	−8.95
0.00	70% ank, 30% sid	−10.91

The stratigraphic position of the data indicated by mm corresponds to Fig. 5. The carbonate composition is inferred from estimated modal abundances of calcite, sid = siderite and ank = ankerite.

5.1.2. Formation of hematite from ferric oxyhydroxide

In virtually unmetamorphosed BIFs, hematite is an early diagenetic product formed by dehydration of a ferric oxyhydroxide precursor (e.g. Klein, 2005). Ferric oxyhydroxide, in turn, is considered to originate from oxidation of $Fe(II)_{aq}$ in surface waters followed by settling of particles through Fe(II)-rich anoxic bottom water.

Oxidation of $Fe(II)_{aq}$ is suggested to be caused by anaerobic photosynthesis (e.g. Widdel et al., 1993; Konhauser et al., 2002; Kappler et al., 2005) or by dissolved oxygen in the upper ocean (e.g. Holland, 1973; Drever, 1974; Ehrenreich and Widdel, 1994; Kaufman et al., 2007). UV photo-oxidation has also been considered as possible mechanism (e.g. Cairns-Smith, 1978), but has been recently discounted as the cause of efficient Fe precipitation (Konhauser et al., 2007b). Both mechanisms precipitate ferric hydr(oxide) with a Fe isotope composition that is around 1.5‰ heavier than Fe(II) in seawater (Bullen et al., 2001; Skulan et al., 2002; Welch et al., 2003; Croal et al., 2004; Anbar et al., 2005). Such isotope fractionation will become apparent in the ferric product only if a small quantity of Fe(II) is oxidized (i.e. partial Fe(II) oxidation). In contrast, when 100% of the Fe(II) is oxidized, the ferric product would have obtained the isotope signature of the seawater. In this case, the isotope signature of the seawater would have been transferred into the precipitate.

Yet even if the settling precipitate obtained the seawater's Fe isotope composition, it would evolve towards heavier Fe compositions during settling through Fe-rich bottom water. Several experimental studies indicate that Fe(II) adsorption on Fe oxides is commonly followed by atomic exchange and attains isotope equilibrium within weeks (Pedersen et al., 2005; Jang et al., 2008; Handler et al., 2009; Mikutta et al., 2009). In this case, the precipitated ferric hydr(oxide) carries a Fe isotope signature that is up to 1.5‰ heavier than seawater (Bullen et al., 2001; Skulan et al., 2002; Welch et al., 2003; Croal et al., 2004; Anbar et al., 2005).

In any case, hematite, the ultimate product, likely preserves the isotope composition of oxides attained in the water column. We have to bear in mind, however, that diagenetic alteration of this isotope signature might have taken place. During diagenesis, biotic or abiotic reduction of ferric (hydr)oxide and the subsequent release of $Fe(II)_{aq}$ with a negative Fe isotope composition into pore fluids can shift the isotope signature of the residues to higher δ^{56}Fe values (Crosby et al., 2005, 2007; Pedersen et al., 2005; Severmann et al., 2006; Staubwasser et al., 2006; Severmann et al., 2008; Homoky et al., 2009). Since ferric (hydr)oxide reduction is linked to the availability of organic carbon, which likely varies between layers, we expect the diagenetic process to change the Fe isotope composition of Fe oxides between layers. Bearing this effect in mind, the negligible vertical variability of the Fe isotope composition of hematite in core sections 3/79 and DGM-36 suggests that the isotope composition is primary (Fig. 3). Furthermore, the difference in δ^{56}Fe between hematite and coexisting magne-

Table 4
Si isotope data of chert in the investigated BIFs obtained by LA-MC-ICP-MS.

mm	$\delta^{29}Si$	$\delta^{30}Si$
Dales Gorge Member DGM-36 (Hamersley)		
38.52	−0.66 ± 0.08	−1.09 ± 0.09
38.12	−0.57 ± 0.05	−1.01 ± 0.07
37.88	−0.61 ± 0.08	−1.29 ± 0.12
	−0.48 ± 0.08	−0.93 ± 0.10
37.64	−0.43 ± 0.07	−0.95 ±0.10
37.16	−0.48 ± 0.06	−0.91 ± 0.07
36.68	−0.51 ± 0.08	−1.04 ± 0.10
35.24	−0.37 ± 0.09	−0.92 ± 0.11
33.80	−0.50 ± 0.08	−1.19 ± 0.11
33.56	−0.60 ± 0.08	−1.38 ± 0.12
29.32	−0.68 ± 0.09	−1.60 ± 0.11
	−0.62 ± 0.08	−1.46 ± 0.11
27.88	−0.71 ± 0.09	−1.58 ± 0.11
26.76	−0.67 ± 0.08	−1.40 ± 0.12
25.64	−0.68 ± 0.08	−1.34 ± 0.11
23.64	−0.59 ± 0.08	−1.33 ± 0.11
23.08	−0.75 ± 0.09	−1.51 ± 0.15
20.04	−0.76 ± 0.09	−1.57 ± 0.15
18.68	−0.66 ± 0.06	−1.37 ± 0.09
17.96	−0.58 ± 0.07	−1.11 ± 0.10
16.44	−0.67 ± 0.07	−1.27 ± 0.09
15.24	−0.67 ± 0.07	−1.41 ± 0.11
14.44	−0.62 ± 0.08	−1.19 ± 0.09
14.60	−0.77 ± 0.10	−1.53 ± 0.16
13.40	−0.56 ± 0.07	−1.15 ± 0.09
13.36	−0.68 ± 0.08	−1.21 ± 0.11
10.80	−0.50 ± 0.08	−1.09 ± 0.11
8.96	−0.47 ± 0.08	−1.02 ± 0.11
7.76	−0.61 ± 0.09	−1.37 ± 0.13
	−0.50 ± 0.08	−1.09 ± 0.10
6.16	−0.61 ± 0.08	−1.30 ± 0.13
4.80	−0.67 ± 0.07	−1.40 ± 0.11
2.88	−0.60 ± 0.07	−1.23 ± 0.12
2.56	−0.59 ± 0.07	−1.33 ± 0.10
0.96	−0.50 ± 0.07	−1.08 ± 0.09
0.00	−0.61 ± 0.07	−1.27 ± 0.10
Kuruman Iron Formation 3/59 (Transvaal)		
40.20	−0.54 ± 0.07	−1.19 ± 0.14
39.37	−0.62 ± 0.07	−1.38 ± 0.15
38.71	−0.76 ± 0.09	−1.37 ± 0.17
38.05	−0.55 ± 0.07	−1.09 ± 0.12
	−0.61 ± 0.07	−1.13 ± 0.13
37.84	−0.59 ± 0.06	−1.16 ± 0.12
32.84	−0.55 ±0.11	−0.95 ±0.19
20.80	−0.66 ± 0.07	−1.33 ± 0.14
20.40	−0.72 ± 0.08	−1.54 ± 0.13
19.82	−0.66 ± 0.06	−1.38 ± 0.13
18.88	−0.52 ± 0.07	−1.08 ± 0.11
18.46	−0.61 ± 0.03	−1.22 ± 0.06
17.25	−0.56 ± 0.04	−1.06 ± 0.08
16.71	−0.61 ± 0.04	−1.02 ± 0.08
16.35	−0.57 ± 0.03	−1.17 ± 0.06
15.81	−0.65 ± 0.06	−1.32 ± 0.14
15.38	−0.66 ± 0.07	−1.40 ± 0.15
14.50	−0.59 ± 0.04	−1.33 ± 0.04
13.62	−0.55 ± 0.05	−1.25 ± 0.06
12.16	−0.60 ± 0.07	−1.22 ± 0.15
10.97	−0.59 ± 0.07	−1.27 ± 0.15
9.90	−0.44 ± 0.04	−0.98 ± 0.08
9.51	−0.51 ± 0.07	−1.14 ± 0.12
8.10	−0.47 ± 0.03	−0.96 ± 0.05
7.78	−0.69 ± 0.05	−1.28 ± 0.07
5.08	−0.75 ± 0.06	−1.41 ± 0.16
0.00	−0.72 ± 0.08	−1.27 ± 0.16
Kuruman Iron Formation 3/79 (Transvaal)		
31.10	−0.40 ± 0.07	−0.83 ± 0.11
	−0.35 ± 0.04	−0.87 ± 0.07
	−0.47 ± 0.08	−0.96 ± 0.09
30.25	−0.48 ± 0.07	−0.97 ± 0.08
27.85	−0.45 ± 0.03	−0.92 ± 0.06
26.03	−0.34 ± 0.08	−0.82 ± 0.12
25.14	−0.35 ± 0.08	−0.87 ± 0.13
25.30	−0.40 ± 0.04	−0.94 ± 0.06
25.31	−0.47 ± 0.07	−0.96 ± 0.12
26.61	−0.40 ± 0.08	−0.85 ± 0.12
27.29	−0.46 ± 0.04	−1.04 ± 0.08
22.59	−0.41 ± 0.04	−0.84 ± 0.06
21.00	−0.49 ± 0.04	−0.88 ± 0.08
20.03	−0.50 ± 0.07	−0.79 ± 0.14
19.38	−0.45 ± 0.08	−0.77 ± 0.14
18.42	−0.45 ± 0.03	−0.84 ± 0.07
17.95	−0.39 ± 0.07	−0.62 ± 0.13
17.20	−0.35 ± 0.07	−0.73 ± 0.14
16.10	−0.46 ± 0.06	−0.73 ± 0.14
13.40	−0.37 ± 0.08	−0.75 ± 0.17
12.00	−0.35 ± 0.07	−0.62 ± 0.16
10.55	−0.36 ± 0.08	−0.70 ± 0.17
10.15	−0.45 ± 0.07	−0.90 ± 0.21
8.97	−0.50 ± 0.07	−0.94 ± 0.15
7.95	−0.34 ± 0.08	−0.76 ± 0.15
6.65	−0.48 ± 0.08	−0.79 ± 0.17
4.50	−0.42 ± 0.07	−0.77 ± 0.15
3.92	−0.46 ± 0.08	−0.72 ± 0.17
3.37	−0.40 ± 0.08	−0.84 ± 0.17
2.90	−0.35 ± 0.04	−0.64 ± 0.05
0.15	−0.33 ± 0.04	−0.63 ± 0.06
Penge Iron Formation TBT (Transvaal)		
32.85	−0.34 ± 0.07	−0.70 ± 0.11
31.92	−0.38 ± 0.07	−0.82 ± 0.13
30.60	−0.32 ± 0.07	−0.74 ± 0.14
29.55	−0.38 ± 0.07	−0.85 ± 0.13
28.90	−0.35 ± 0.06	−0.80 ± 0.13
27.68	−0.38 ± 0.07	−0.92 ± 0.13
25.75	−0.41 ± 0.08	−1.01 ± 0.23
24.90	−0.33 ± 0.07	−0.65 ± 0.18
23.45	−0.22 ± 0.07	−0.61 ± 0.13
	−0.29 ± 0.07	−0.70 ± 0.13
	−0.42 ± 0.07	−0.85 ± 0.15
22.10	−0.40 ± 0.08	−0.51 ± 0.20
20.24	−0.46 ± 0.07	−0.68 ± 0.17
19.10	−0.37 ± 0.07	−0.82 ± 0.11
17.95	−0.44 ± 0.06	−0.82 ± 0.13
16.25	−0.51 ± 0.06	−0.83 ± 0.12
15.80	−0.37 ± 0.07	−0.74 ± 0.15
16.25	−0.39 ± 0.07	−0.65 ± 0.13
13.78	−0.40 ± 0.07	−0.78 ± 0.14
12.10	−0.31 ± 0.08	−0.71 ± 0.16
10.95	−0.41 ± 0.07	−0.92 ± 0.13
9.15	−0.48 ± 0.08	−1.02 ± 0.14
8.76	−0.49 ± 0.07	−1.04 ± 0.14

Table 4 (*continued*)

mm	$\delta^{29}Si$	$\delta^{30}Si$
7.90	-0.38 ± 0.08	-0.76 ± 0.14
7.05	-0.28 ± 0.07	-0.53 ± 0.14
6.34	-0.35 ± 0.04	-0.84 ± 0.06
5.23	-0.43 ± 0.07	-0.79 ± 0.13
3.00	-0.35 ± 0.05	-0.54 ± 0.08
2.82	-0.40 ± 0.08	-0.72 ± 0.14
0.90	-0.39 ± 0.04	-0.84 ± 0.07
0.00	-0.43 ± 0.04	-0.75 ± 0.08

The stratigraphic positions of the analyses are indicated by mm corresponding to Fig. 3. Uncertainties of single analysis are given by 2 standard errors.

tite, a likely diagenetic product, is variable suggesting that hematite or its precursor have conserved the original isotope ratio, while the isotope fractionation associated with Fe(III) reduction is recorded in magnetite. Therefore, the Fe isotope composition of hematite is considered to be unaltered and can be used to infer processes in the water column. Hematite in samples 3/79 and DGM-36 reveals uniform $\delta^{56}Fe$ values of ~0‰ and ~−0.8‰, respectively, providing at least upper limits for the seawater composition at the time of deposition.

5.1.3. Primary siderite precipitation

Several authors have suggested primary siderite precipitation during the formation of BIFs (e.g. Klein and Beukes, 1989; Kaufman et al., 1990; Sumner, 1997). The concentration of dissolved Fe(II) may increase with depth in the ocean, which slows down calcite precipitation and triggers supersaturation of dissolved Fe(II) with respect to siderite. Siderite then precipitates directly from the water column. According to the results of the experimental work of Wiesli et al. (2004), siderite is ~0.5‰ lighter in its Fe isotope composition than dissolved Fe(II), from which it precipitates under equilibrium conditions.

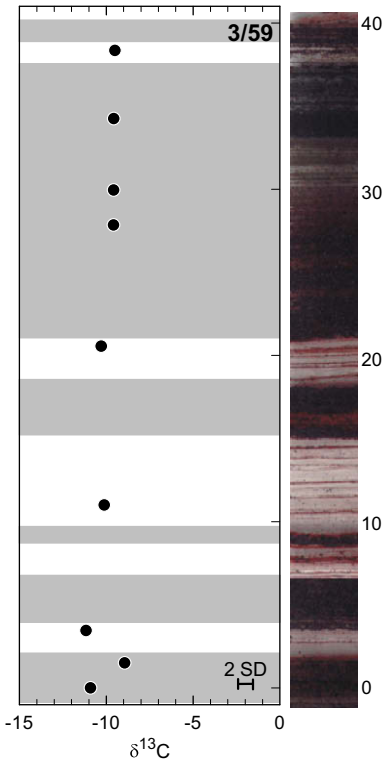

Fig. 5. Carbon isotope composition of sample 3/59 from the Kuruman Iron Formation, Transvaal (South Africa). Despite variable chemical composition of Fe carbonates, the C isotope composition is largely homogeneous indicating a mixed carbon source of inorganic and organic origin.

The differences in $\delta^{56}Fe$ among coexisting magnetite and Fe carbonate phases in individual layers of sample 3/59 are variable at 0.1‰ to 0.6‰ and inconsistent with suggested magnetite–siderite fractionation factors ranging between 0.8‰ and 1.8% (Polyakov and Mineev, 2000; Mineev et al., 2007; Polyakov et al., 2007; Johnson et al., 2008a) (see Section 5.1.4 and Fig. 3). This observation implies isotopic disequilibrium. Hence, formation pathways for magnetite and Fe carbonates were decoupled. Siderite has a uniform $\delta^{56}Fe$ value of ~−0.7‰ in this core section, which, if primary, is consistent with a steady seawater composition of −0.2‰ based on the fractionation factor siderite–$Fe(II)_{aq}$ of −0.5‰ (Wiesli et al., 2004). Ankerite and Mg-rich siderite exhibit lower $\delta^{56}Fe$ values ranging from −1.2‰ to −0.7‰. This depletion is likely a diagenetic effect as these carbonates are considered as diagenetically altered phases formed at the expense of siderite (Kaufman et al., 1990).

Carbon isotope signatures provide additional information about the processes of carbonate formation. Regardless of the chemical composition of carbonates in layers of sample 3/59, $\delta^{13}C$ values are largely constant around −10‰, which is in the range of previously investigated BIFs of the Transvaal succession with $\delta^{13}C$ values between −14‰ and −3‰ (Beukes and Klein, 1990; Beukes et al., 1990; Kaufman, 1996; Fischer et al., 2009). The range in BIFs have been interpreted to reflect variable pathways for C in carbonates (Veizer et al., 1989; Beukes and Klein, 1990; Beukes et al., 1990; Kaufman et al., 1990; Kaufman, 1996; Fischer et al., 2009). Relatively high $\delta^{13}C$ values are considered to reflect precipitation of carbonates from seawater with a 'mantle-like' composition. Carbonates with significant negative $\delta^{13}C$ values have been suggested to carry carbon predominately released from diagenetic organic matter degradation accompanied by Fe(III) reduction. Considering both, the Fe and C isotope signatures in sample 3/59, the carbonate phases are likely derived from primary siderite, which precipitated from seawater dominated by inorganic carbon but also contained some dissolved organic carbon.

5.1.4. Diagenetic siderite and magnetite formation

It is widely assumed that the diagenetic formation of siderite and magnetite occurs due to reduction of ferric (hydr)oxides as organic carbon is oxidized (e.g. Han, 1978; Ewers and Morris, 1981; Lovley, 1991). The $Fe(II)_{aq}$ released reacts either with residual ferric (hydr)oxide to form magnetite or with bicarbonate to produce siderite. This conversion is either catalysed by DIR during early diagenesis or is an abiotic spontaneous reaction at late diagenesis or low-grade metamorphism (e.g. Lovley, 1991). Iron isotope fractionation and the kinetics of isotope exchange in a system

involving DIR have been investigated in detail (Crosby et al., 2005, 2007; Johnson et al., 2005). In contrast, the fractionation in the abiotic system is largely unknown. Magnetite and siderite that formed contemporaneously should reflect the equilibrium magnetite–siderite fractionation factor. This factor is estimated to be 1.8‰ for the pathway involving DIR by experimental studies (Johnson et al., 2008a and references therein) and decreases to 1.6‰ to 0.8‰ for abiotic reduction at temperatures between 120 and 170 °C as predicted from Mössbauer data (Polyakov and Mineev, 2000; Mineev et al., 2007; Polyakov et al., 2007).

Coupled diagenetic formation of magnetite and siderite by biotic or abiotic Fe(III) reduction is a likely process in sample DGM-36 (Fig. 3). Even though the magnetite–siderite assemblage could not be measured in direct contact at many locations, both minerals show uniform Fe isotope compositions giving an overall difference of ~1.2‰. The similar Fe isotope composition of magnetite and hematite in this sample can be explained by the low abundance of siderite. Released $Fe(II)_{aq}$ due to reduction is nearly quantitatively incorporated into magnetite and only to a much lesser extent into the rare occurrences of siderite. Therefore, mass balance dictates that the Fe isotope composition of magnetite and hematite is virtually indistinguishable. Hence, the low $\delta^{56}Fe$ values of magnetite are inherited from the ferric (hydr)oxide precursor.

In samples 3/79 and 3/59, diagenetic processes would have only formed magnetite from a ferric (hydr)oxides precursor. Magnetite is isotopically lighter than hematite in sample 3/79 and also lighter than an inferred ferric (hydr)oxide composition in sample 3/59. A minimum $\delta^{56}Fe$ value for a ferric (hydr)oxide precursor for sample 3/59 can be estimated as it equals the derived seawater composition of −0.2‰ (see Section 5.2.2). Therefore, magnetite formation form a ferric (hydr)oxide precursor in these samples was accompanied either by loss of isotopically heavy Fe or gain of isotopically light Fe.

There are two possible mechanisms: loss of heavy Fe isotopes can take place when magnetite forms by abiotic reduction of a ferric (hydr)oxide precursor. Approaches using Mössbauer data propose 0.1‰ to −0.5‰ for the equilibrium magnetite–$Fe(II)_{aq}$ fractionation factor at ambient temperatures (Anbar et al., 2005; Mineev et al., 2007; Polyakov et al., 2007). Hence, magnetite evolves towards lighter Fe isotope composition than the original Fe(III) substrate, depending on the amount of isotopically heavy $Fe(II)_{aq}$ loss. Gain of light Fe isotopes into magnetite can take place by non-redox reactions of a ferric (hydr)oxide precursor with $Fe(II)_{aq}$ (Ohmoto, 2003). For instance, isotopically light $Fe(II)_{aq}$ derived from DIR that would have been released elsewhere diffused into the sediment resulting in magnetite with low $\delta^{56}Fe$ values (Johnson et al., 2008a).

5.1.5. Replacement of magnetite by hematite in metamorphosed BIF

Sample TBT from Penge Iron Formation of the Transvaal succession represents an altered BIF, which was effected by contact metamorphism owing to the Bushveld intrusion and later hydrothermal oxidative fluid infiltrations (Gutzmer et al., 2005). In this sample, hematite has most likely replaced magnetite during hydrothermal iron ore formation. Magnetite preserves its original Fe isotope composition throughout prograde contact metamorphism (Frost et al., 2007). Oxidative metasomatism is unlikely to mobilize Fe. Therefore magnetite is likely to have been quantitatively transformed into hematite without significant Fe redistribution, which preserves the original Fe isotope composition. Hence, the Fe isotope composition in hematite of ~−0.4‰ for $\delta^{56}Fe$ reflects the Fe isotope signature of the original magnetite, which likely formed during diagenesis by one of the processes discussed above.

5.1.6. Small-scale heterogeneities

Fe oxide minerals exhibit small-scale heterogeneities in the Fe isotope composition including both lateral and vertical variations.

(1) In sample 3/79, magnetite exhibits a homogeneous Fe isotope composition within a given Fe oxide-rich layer but is variable between layers. In contrast, its mineralogical precursor, hematite, shows a uniform Fe isotope composition (Fig. 3d). These observations suggest a diagenetic origin for this variability. The inter-layer variability implies that diagenetic fluids have dispersed mainly laterally and supports that significant Fe exchange across layering is absent in BIFs (Frost et al., 2007; Johnson et al., 2008a; Steinhoefel et al., 2009a). The homogeneous Fe isotope composition of magnetite within layers suggests magnetite formation under $Fe(II)_{aq}$ excess conditions.
(2) In vertical direction, shifts in the Fe isotope composition of magnetite within a few microns as observed in sample 3/59 (Figs. 1c and 3h) suggest a pre-depositional origin as diagenetic fluids would decrease rather than increase the range of isotope compositions on the micrometer scale. It is unlikely that these small-scale heterogeneities reflect variable seawater composition as the assumed long residence time of Fe would have prohibited short-term changes (Johnson et al., 2008a). Moreover, the identification of primary siderite in this sample suggests a constant seawater composition for the period represented by the investigated core section (see Section 5.1.3). Small-scale isotope heterogeneity in magnetite is most likely inherited from its precursor reflecting variable degrees of partial Fe(II) oxidation in the upper water column.
(3) In lateral direction, slight variations of the Fe isotope composition in both hematite and magnetite as observed in sample DGM-36 (Fig. 3j) can have both a primary or diagenetic origin. Variable oxidation and Fe(II) adsorption rates within the water column or diagenetic effects (Crosby et al., 2007) could have caused the variability in the Fe isotope composition.
(4) Lateral heterogeneities in magnetite can also result from $Fe(II)_{aq}$-limiting conditions during crystallization. Reservoir effects in pore fluids have been invoked for isotopically zoned magnetite crystals observed in the Archean Old Wanderer BIF (Stein-

hoefel et al., 2009a and Fig. 4) and heterogeneities as found in Isua BIFs (Whitehouse and Fedo, 2007). During metamorphism, the heterogeneity of magnetite can be passed on to secondary hematite. For example in sample TBT, hematite formed from magnetite by an oxidative hydrothermal fluid event related to the Bushveld intrusion; its Fe isotope variability might have been inherited from a heterogeneous magnetite precursor.

5.2. Seawater to sediment cycling of Si and Fe

The Fe and Si isotope signatures for the seawater inferred from these cores are constant for the deposition time of each individual core section. The absence of short-term variations is consistent with the suggested long residence time of Si and Fe in the order of 10^5 to 10^6 years (Siever, 1992; Trendall, 2002). These conditions are characteristic of the typical depositional setting of Proterozoic BIFs on partially isolated continental shelf platforms. These areas are removed from the direct influence of either hydrothermal venting systems or continental drainage (e.g. Klein, 2005). In this regard, Proterozoic BIFs differ from Archean BIFs associated with greenstone belts. For instance, the 2.7 Ga Old Wanderer BIF within the Shurugwi Greenstone Belt (Zimbabwe) shows correlated small-scale variations in Si and Fe isotope signatures of bulk layers, which have been interpreted to reflect the dynamics of hydrothermal emanation (Fig. 6, Steinhoefel et al., 2009a).

Considering the bulk layer Si and Fe isotope composition of the BIFs investigated here, both systems exhibit lower isotope ratios as compared to assumed source composition (Fig. 6). The Fe supply to the ocean by hydrothermal fluids and, to a minor extent, continental drainage (e.g. Jacobsen and Pimentel-Klose, 1988; Canfield, 1998) has been suggested to have carried a Fe isotope composition between −0.4‰ and 0.1‰ (Yamaguchi et al., 2005). The Si supply by hydrothermal fluids would have carried a Si isotope signature of near-zero, whereas continental weathering delivered Si with a Si isotope signature of ~1‰ as inferred from modern sources (De La Rocha et al., 2000; Hamade et al., 2003; Maliva et al., 2005; Georg et al., 2006, 2009).

This apparent disequilibrium between the Fe and Si isotope compositions of the influx and the outflux, i.e. the deposited BIFs, is incompatible with a simple steady state model for the ocean basin. Fig. 7 presents a conceptual model for Si and Fe precipitation and defines two end-member scenarios for a Precambrian ocean basin: non-steady state and steady state conditions. In the first case, the isotope composition of seawater equals that of the input. The isotope signature of the output, i.e. the deposited BIFs, reflects then the overall solution–precipitate fractionation factors. Assumed fractionation factors of −1.5‰ for silica gel (De La Rocha et al., 1997; Ziegler et al., 2005; Basile-Doelsch, 2006; Delstanche et al., 2009) and 1.5‰ for ferric oxyhydroxide (Bullen et al., 2001; Skulan et al., 2002; Welch et al., 2003; Croal et al., 2004; Anbar et al., 2005) precipitation from solution, respectively, would lead to overall negative δ^{30}Si and positive δ^{56}Fe values in BIFs (see also Fig. 6). In the steady state case, both quantity and isotope composition of the outflux correspond to the influx implying that deposited BIFs carry the Si and the

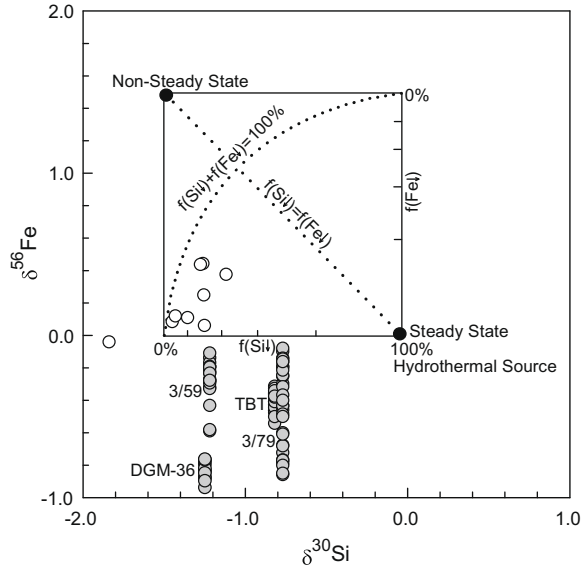

Fig. 6. Hypothetical model for δ^{30}Si and δ^{56}Fe of initial precipitates, silica and ferric oxyhydroxide depending on the precipitated fraction f (modified after Steinhoefel et al., 2009a). Precipitation takes place from seawater with a hypothetical hydrothermal signature with δ^{56}Fe and δ^{30}Si of 0‰, respectively. Ferric oxyhydroxide is 1.5‰ heavier in δ^{56}Fe, whereas SiO_2 is 1.5‰ lighter compared to seawater. Two end-member scenarios can be defined: (1) The isotope composition of the depositional outflux corresponds to the hydrothermal influx of 0‰, which is realized either by steady state conditions or 100% precipitation of the dissolved Fe and Si. (2) Precipitation of small fractions from seawater with a hydrothermal signature results in isotope compositions reflecting the fractionation factors of −1.5‰ in δ^{30}Si (De La Rocha et al., 1997; Ziegler et al., 2005; Basile-Doelsch, 2006) and 1.5‰ in δ^{56}Fe (Bullen et al., 2001; Skulan et al., 2002; Welch et al., 2003; Croal et al., 2004; Anbar et al., 2005) representing non-steady state conditions. The diagonal dotted line shows the isotope evolution by Rayleigh distillation for precipitating equal fractions of dissolved Si and Fe (f(Si↓) = f(Fe↓)). The dotted curve illustrates the trend of opposite fractions of cumulative precipitated Si and Fe (f(Si↓) + f(Fe↓) = 100%). The axes of the inset indicate the removed fractions of Fe and Si. The Archean Old Wanderer BIF from the 2.7 Ga Shurugwi Greenstone Belt (Zimbabwe) (open cycles) exhibits covariable Si and Fe isotope data for bulk layers, which plot roughly along the curve of opposite fractions of cumulative precipitated Si and Fe (Steinhoefel et al., 2009a). This feature has been interpreted as direct influence on Si and Fe precipitation by hydrothermal activity (for details see Steinhoefel et al. (2009a)). In contrast, the estimated bulk layer compositions of the Proterozoic Hamersley-Transvaal BIFs (grey cycles) plot below the quadrant of expected Si and Fe isotope composition and show independent Si and Fe isotope signatures. The low but uniform Si isotope signatures suggest precipitation at constant conditions indicating either non-steady state conditions or a complementary sink of isotopically heavy Si. The low δ^{56}Fe values imply isotopically light seawater or diagenetic alteration towards lower δ^{56}Fe (see Section 5 for details).

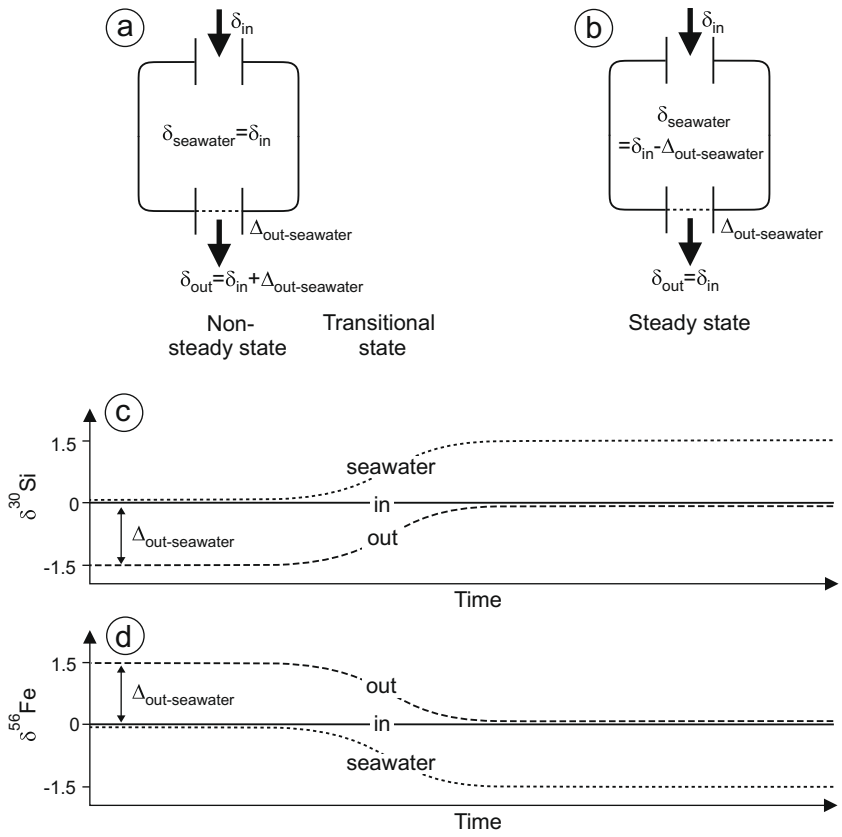

Fig. 7. Conceptual models for the temporal evolution of the Fe and Si isotope composition in an ocean basin. The ocean basin presents a single compartment with no isotope fractionation at intake, but isotope fractionation at precipitation into sediment with an associated isotope fractionation factor $\Delta_{out\text{-}seawater}$. (a) At non-steady state, the isotope composition of seawater $\delta_{seawater}$ equals that of the influx δ_{in}. The isotope composition of the outflux δ_{out}, i.e. the precipitated Fe and Si, is determined by $\delta_{seawater}$ and $\Delta_{out\text{-}seawater}$. (b) At steady state, the influx equals the outflux in quantity and isotope composition. Hence, $\delta_{seawater}$ evolves towards $\delta_{in} - \Delta_{out\text{-}seawater}$. In (c and d), the temporal evolution of Fe and Si isotope signatures of the influx, the seawater and the outflux are delineated as the system evolves from non-steady state to steady state conditions. Here, we assume fractionation factors of $-1.5‰$ and $1.5‰$ for silica gel and ferric oxyhydroxide from solution (De La Rocha et al., 1997; Bullen et al., 2001; Skulan et al., 2002; Welch et al., 2003; Croal et al., 2004; Anbar et al., 2005; Ziegler et al., 2005; Basile-Doelsch, 2006), respectively, and an isotope composition of $0‰$ for both sources, Fe and Si (De La Rocha et al., 2000; Yamaguchi et al., 2005). This temporal evolution is not a Rayleigh type process.

Fe isotope composition of the sources. The isotope compositions of the seawater and the precipitates adapt according to the associated fractionation factor for Si and Fe (Fig. 7c and d).

However, the isotope compositions of the investigated BIFs are far away from their potential steady state position (Fig. 6). For the BIF samples investigated, we are able to estimate the Fe and Si isotope composition of the influx, the seawater and the outflux, i.e. the deposited BIFs, to evaluate the Si and Fe isotope mass balance of the ancient ocean basin at the time of deposition of these samples.

5.2.1. Si fluxes

Non-steady state conditions in the ocean basins could have prevailed if the BIF genesis was related to extraordinarily strong hydrothermal activity or continental weathering (see discussion in Maliva et al. (2005)), which increased the Si influx into the basin temporally. In this case, the seawater would have carried the isotope signature of the source, but the deposits would have obtained a Si isotope signature different from that of the source due to fractionation during precipitation, which favours light Si isotopes (Fig. 7a) (De La Rocha et al., 1997; Ziegler et al., 2005; Basile-Doelsch, 2006; Delstanche et al., 2009). If this is the case, differences in the Si isotope composition between different BIF samples can be explained by variable contributions from hydrothermal and terrigeneous Si. Chert with strongly negative δ^{30}Si values, such as found in samples 3/59 and DGM-36 with mean δ^{30}Si values of $-1.22‰$ and $-1.25‰$, respectively, are close to the Si isotope composition of modern siliceous deposits around oceanic smokers with an average δ^{30}Si values of $-1.56‰$ as based on 25 measurements (Ding et al., 1996). The inferred seawater composition from these samples of about $0.3‰$ in δ^{30}Si (see Section 5.1.1) also indicates a significant hydrothermal influence. Chert with comparatively higher δ^{30}Si values, i.e. sample 3/79 with a mean δ^{30}Si values of $-0.77‰$, suggest an enhanced terrigeneous influence. The inferred seawater

composition of about 0.7‰ corresponds to the Si isotope signature of Si released by modern continental weathering (Georg et al., 2006, 2009). Another explanation for the Si isotope differences between cores is an ocean basin that is in a transitional stage. Then, strongly negative δ^{30}Si values in chert reflect seawater dominated by a hydrothermal influence, while moderately negative values indicate a development away from the hydrothermal signature back to steady state conditions (Fig. 7c).

Steady state conditions for the ocean basin are also compatible with the Si isotope signatures of these BIFs if two sinks for Si existed. In this model, chert in BIFs represents the sink of isotopically light Si, whereas the heavy counterpart is deposited elsewhere (Fig. 8). Positive δ^{30}Si values have been reported for some Precambrian marine chert deposits, indicating that this complementary sink might exist (Robert and Chaussidon, 2006; van den Boorn et al., 2007, 2010; Abraham et al., 2009; Chakrabarti et al., 2009).

Both scenarios, steady state conditions with two complementary Si sinks as well as non-steady state conditions, appear possible for a Precambrian ocean basin. Further investigations need to explore the spatial distribution as well as temporal variations of Si isotope signature of chert deposits to evaluate, which model represents the conditions of a Precambrian ocean basin.

5.2.2. Fe fluxes

While the overall Fe isotope composition of the Hamersley and Transvaal BIFs of close to 0‰ seems in balance with the influx composition of −0.4‰ to 0.1‰ (Yamaguchi et al., 2005; Johnson et al., 2008a), that of the samples investigated here are not. In the long-term records, the major Fe-bearing mineral phases in unmetamorphosed BIFs, magnetite and Fe carbonate, exhibit large variations.

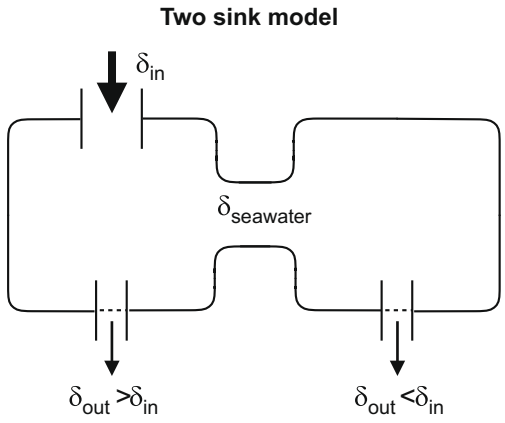

Fig. 8. Steady state ocean model for Si and Fe considering two sinks. The in- and outfluxes of the ocean basin would have been in balance if complementary sinks for heavy Si and Fe isotopes existed. The negative Si isotope of BIFs is likely balanced by deposition of heavy Si isotopes in other chert deposits within the ocean basin. For Fe, microbial carbonates, shales and sedimentary pyrites and in part BIFs represents the sink for light Fe isotopes (Johnson et al., 2003, 2008a; Rouxel et al., 2005; Yamaguchi et al., 2005; von Blanckenburg et al., 2008; this study), whereas the heavy counterpart might have been deposited in pelagic sediments, which are not preserved.

δ^{56}Fe values of magnetite in bulk layers range from −1.1‰ to 1.3‰ with an average of -0.1 ± 0.9‰ (2 SD, $n = 120$), whereas δ^{56}Fe values of Fe carbonates in bulk layers vary between −2.2‰ and 1.1‰ giving an average of -0.6 ± 1.1‰ (2 SD, $n = 100$) (Johnson et al., 2003, 2008a; this study). The samples investigated here are all on the lower end of the Fe isotope range as mapped out for longer periods (Fig. 9). Furthermore, other Fe sinks in Precambrian ocean basins including microbial carbonates, organic-rich shales and sedimentary pyrites are also depleted in heavy Fe isotopes (Rouxel et al., 2005; Yamaguchi et al., 2005; von Blanckenburg et al., 2008).

The first possibility evaluated here is that the low δ^{56}Fe values in BIFs are the result of diagenetic isotope fractionation. As it has been shown in Section 5.1, in both Kuruman samples 3/79 and 3/59, magnetite with low δ^{56}Fe values was formed by post-depositional supply of isotopically light Fe(II) or diffusive loss of isotopically heavy Fe(II). In sample 3/59, Fe isotope fractionation during precipitation of primary siderite adds to the overall negative Fe isotope signature.

A second possibility is apparent from the core section from the Dales Gorge Member DGM-36. This sample reveals a constant Fe isotope composition of ~−0.8‰ (magnetite and hematite are the major Fe-bearing phases). Since this BIF likely formed by complete Fe(II) oxidation during ferric oxyhydroxide precipitation, the overall negative Fe isotope composition of this sample is inherited from the seawater. Fe recycled from sediments by DIR could be a Fe source, in a similar manner to modern shelf areas, that release large quantities of $Fe(II)_{aq}$ with low δ^{56}Fe values down to −3.3‰ (Bergquist and Boyle, 2006; Severmann et al., 2006, 2008 Staubwasser et al., 2006; Homoky et al., 2009). Addition of such a pulse of light Fe isotopes might have been a transient phenomenon, which would have shifted the basin's Fe Budget out of steady state (Fig. 7d).

A third possibility is that low δ^{56}Fe was present in seawater because isotopically heavy Fe was deposited by oxidation of $Fe(II)_{aq}$ elsewhere, leaving an isotopically light dissolved Fe residue behind (Rouxel et al., 2005). This scenario is also compatible with the finding of low δ^{56}Fe values in microbial carbonates in the Early Proterozoic (von Blanckenburg et al., 2008). These carbonates require light Fe isotopes in seawater, yet their lanthanide compositions show no sign of a diagenetic imprint. All these scenarios, however, require a sink for high δ^{56}Fe to exist for a steady state ocean model. Considering only BIFs, of which the long-term records appear to represent the suggested influx, these two sinks could be presented by the synchronous formation of both isotopically light and heavy BIFs in adjacent deposits. Taking into account that many other deposits of the Precambrian ocean contain light Fe isotopes (Rouxel et al., 2005; Yamaguchi et al., 2005; von Blanckenburg et al., 2008), another sink for heavy Fe isotopes must have existed elsewhere (Fig. 8). While such a sink of high δ^{56}Fe is not observed in the geologic record (Johnson et al., 2008b), pelagic sediments might represent this complementary sink, which however are rarely preserved (e.g. Eriksson et al., 2005).

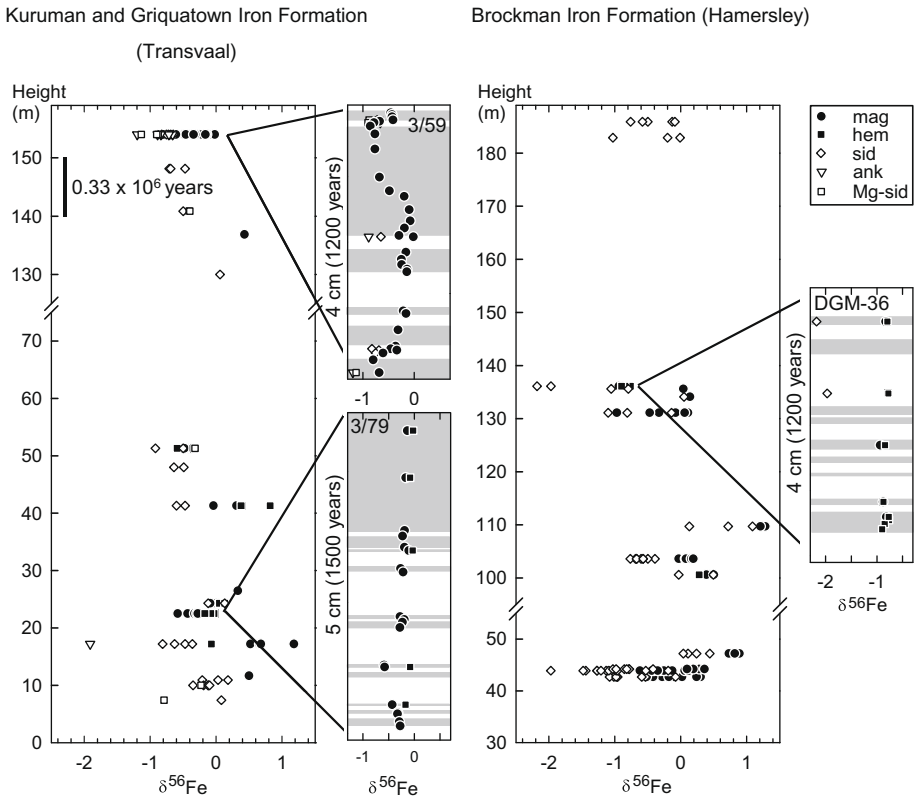

Fig. 9. Fe isotope data of the Kuruman and Griquatown Iron Formation from the Transvaal succession and the simultaneously deposited Brockman Iron Formation from the Hamersley succession including all the data of Johnson et al., 2003; 2008a; this study (modified after Johnson et al. (2008a)). The data represent average Fe isotope values of the different mineral phases in individual layers. The time scale refers to a depositional rate of consolidated sediment of 33 m/10^6 years (Pickard, 2002, 2003). The panels on the right sides scale up the data of this study.

6. CONCLUSIONS

The combined analyses of Si and Fe isotope compositions in the Transvaal–Hamersley BIF deposits suggest distinct pathways of Si and Fe within Proterozoic ocean basins, a conclusion that is in contrast to the observation within the Archean Old Wanderer BIF in the Shurugwi Greenstone Belt (Steinhoefel et al., 2009a). Whereas Si isotope compositions likely represent primary signatures obtained during initial precipitation of Si, Fe isotope compositions can be strongly modified by diagenetic processes. The samples investigated here imply precipitation in a large basin, where the long residence times of Si and Fe in seawater result in high concentrations of these elements, which buffer against the change in seawater ratios within the depositional time scale of these thin sections.

Yet two observations suggest that these depositional areas were not the only sinks for these elements. First Si isotope ratios are much lower than any ratio assumed to represent input from either weathering or hydrothermal sources. Second, Fe isotope ratios in BIFs vary significantly on the long-term record, as shown for instance by the low δ^{56}Fe values in the sections investigate here as compared to the overall Fe isotope composition inferred from long core sections (Johnson et al., 2003, 2008a). Our mineral-scale analytical methods allow us to identify the processes that have led to such low δ^{56}Fe, including diagenetic effects and seawater depleted in heavy Fe isotopes. Furthermore, the record of microbial carbonates, organic-rich shales and sedimentary pyrites shows also low δ^{56}Fe values (Rouxel et al., 2005; Yamaguchi et al., 2005; von Blanckenburg et al., 2008). These observations lead us to suggest that a complementary sink containing the missing heavy isotopes of these elements has existed. For both elements, an attractive explanation is a model with two sinks to maintain steady state in the ocean basin. Peritidal cherts, which are common within Precambrian marine basins, may represent a sink for heavy Si isotopes; however their Si composition needs further investigation. A complementary sink containing heavy Fe isotopes might have been pelagic sediments. Unfortunately, such sediments were rarely preserved in the geological record.

ACKNOWLEDGEMENTS

This research was supported by the DFG and New Wave Research. G.S. is grateful for a scholarship from the University of Hannover. P. Koeniger from the Leibniz Institute for Applied Geophysics in Hannover is thanked for C isotope analyses. O. Dietrich kindly prepared the thin sections. Critical and constructive comments by S. Severmann and two anonymous reviewers greatly improved the manuscript.

REFERENCES

Abraham K., Cardinal D., Hofmann A., Foley S., Harris C. and André L. (2009) The origin of Palaeoarchean silicification inferred from coupled Si–O isotopes. *Geochim. Cosmochim. Acta Goldschmidt Conf. Abstr.* **73**, A4.

Alibert C. and McCulloch M. T. (1993) Rare earth element and neodymium isotopic compositions of the banded iron-formations and associated shales from Hamersley, Western Australia. *Geochim. Cosmochim. Acta* **57**, 187–204.

Anbar A. D., Jarzecki A. A. and Spiro T. G. (2005) Theoretical investigation of iron isotope fractionation between $Fe(H_2O)_6^{3+}$ and $Fe(H_2O)_6^{2+}$: implications for iron stable isotope geochemistry. *Geochim. Cosmochim. Acta* **69**, 825–837.

André L., Cardinal D., Alleman L. Y. and Moorbath S. (2006) Silicon isotopes in 3.8 Ga West Greenland rocks as clues to the Eoarchaean supracrustal Si cycle. *Earth Planet. Sci. Lett.* **245**, 162–173.

Basile-Doelsch I. (2006) Si stable isotopes in the Earth's surface: a review. *J. Geochem. Explor.* **88**, 252–256.

Bau M. and Dulski P. (1992) Small-scale variations of the rare-earth element distribution in Precambrian iron-formations. *Eur. J. Mineral.* **4**, 1429–1433.

Bau M. and Dulski P. (1996) Distribution of yttrium and rare-earth elements in the Penge and Kuruman iron-formations, Transvaal Supergroup, South Africa. *Precambrian Res.* **79**, 37–55.

Bau M., Hohndorf A., Dulski P. and Beukes N. J. (1997) Sources of Precambrian rare-earth elements and iron in Paleoproterozoic iron-formations from the Transvaal Supergroup, South Africa – evidence from neodymium isotopes. *J. Geol.* **105**, 121–129.

Bergquist B. A. and Boyle E. A. (2006) Iron isotopes in the Amazon River system: weathering and transport signatures. *Earth Planet. Sci. Lett.* **248**, 39–53.

Beukes N. J. (1980) Lithofacies and stratigraphy of the Kuruman and Griquatown Iron-formations, northern Cape Province, South Africa. *Trans. Geol. Soc. S. Afr.* **83**, 69–86.

Beukes N. J. and Klein C. (1990) Geochemistry and sedimentology of a facies transition – from microbanded to granular iron-formation – in the Early Proterozoic Transvaal Supergroup, South Africa. *Precambrian Res.* **47**, 99–139.

Beukes N. J., Klein C., Kaufman A. J. and Hayes J. M. (1990) Carbonate petrography, kerogen distribution, and carbon and oxygen isotope variations in an early Proterozoic transition from limestone to iron-formation deposition, Transvaal Supergroup, South Africa. *Econ. Geol.* **85**, 663–690.

Beukes N. and Gutzmer J. (2008) Origin and paleoenvironmental significance of major iron formations at the Archean–Paleoproterozoic boundary. In *Banded Iron Formation-Related High-Grade Iron Ore* (eds. S. Hagemann, C. Rosière, J. Gutzmer and N. J. Beukes). Reviews in Economic Geology, Automated Graphic Systems. pp. 5–47.

Blake T. S. and Barley M. E. (1992) Tectonic evolution of the late Archaean to early Proterozoic Mount Bruce Megasequence set, Western Australia. *Tectonics* **11**, 1415–1425.

Bullen T. D., White A. F., Childs C. W., Vivit D. V. and Schulz M. S. (2001) Demonstration of significant abiotic iron isotope fractionation in nature. *Geology* **29**, 699–702.

Cairns-Smith A. G. (1978) Precambrian solution photochemistry, inverse segregation, and banded-iron formations. *Nature* **276**, 807–808.

Canfield D. E. (1998) A new model for Proterozoic ocean chemistry. *Nature* **396**, 450–453.

Canfield D. E. (2005) The early history of atmospheric oxygen: homage to Robert M. Garrels. *Annu. Rev. Earth Planet. Sci.* **33**, 1–36.

Cheney E. S. (1996) Sequence stratigraphy and plate tectonic significance of the Transvaal succession of southern Africa and its equivalent in Western Australia. *Precambrian Res.* **79**, 3–24.

Chmeleff J., Horn I., Steinhoefel G. and von Blanckenburg F. (2008) In situ determination of precise stable Si isotope ratios by UV-femtosecond laser ablation high-resolution multi-collector ICP-MS. *Chem. Geol.* **249**, 155–166.

Chakrabarti R., Knoll A. H. and Jacobsen S. B. (2009) Silicon isotopic variability in Proterozoic cherts. *Geochim. Cosmochim. Acta Goldschmidt Conf. Abstr.* **73**, A205.

Croal L. R., Johnson C. M., Beard B. L. and Newman D. K. (2004) Iron isotope fractionation by Fe(II)-oxidizing photoautotrophic bacteria. *Geochim. Cosmochim. Acta* **68**, 1227–1242.

Crosby H. A., Johnson C. M., Roden E. E. and Beard B. L. (2005) Coupled Fe(II)–Fe(III) electron and atom exchange as a mechanism for Fe isotope fractionation during dissimilatory iron oxide reduction. *Environ. Sci. Technol.* **39**, 6698–6704.

Crosby H. A., Roden E. E., Johnson C. M. and Beard B. L. (2007) The mechanisms of iron isotope fractionation produced during dissimilatory Fe(III) reduction by *Shewanella putrefaciens* and *Geobacter sulfurreducens*. *Geobiology* **5**, 169–189.

Delstanche S., Opfergelt S., Cardinal D., Elsass F., André L. and Delvaux B. (2009) Silicon isotopic fractionation during adsorption of aqueous monosilicic acid onto iron oxide. *Geochim. Cosmochim. Acta* **73**, 923–934.

Dauphas N., Cates N. L., Mojzsis S. J. and Busigny V. (2007) Identification of chemical sedimentary protoliths using iron isotopes in the >3750 Ma Nuvvuagittuq supracrustal belt, Canada. *Earth Planet. Sci. Lett.* **254**, 358–376.

Dauphas N., van Zuilen M., Wadhwa M., Davis A. M., Marty B. and Janney P. E. (2004) Clues from Fe isotope variations on the origin of early Archean BIFs from Greenland. *Science* **306**, 2077–2080.

De Kock M. O., Evans D. A. D., Gutzmer, J, Beukes, N. J. and Dorland H. C. (2008) Origin and timing of banded iron formation-hosted high-grade hard hematite deposits – a Paleomagnetic approach. In *Banded Iron Formation-Related High-Grade Iron Ore* (eds. S. Hagemann, C. Rosière, J. Gutzmer and N. J. Beukes). Reviews in Economic Geology, Automated Graphic Systems. pp. 48–71.

De La Rocha C. L., Brzezinski M. A. and DeNiro M. J. (1997) Fractionation of silicon isotopes by marine diatoms during biogenic silica formation. *Geochim. Cosmochim. Acta* **61**, 5051–5056.

De La Rocha C. L., Brzezinski M. A. and Deniro M. J. (2000) A first look at the distribution of the stable isotopes of silicon in natural waters. *Geochim. Cosmochim. Acta* **64**, 2467–2477.

Ding T., Jiange S., Wan D., Li Y., Li J., Song H., Liu Z. and Yao X. (1996) *Silicon Isotope Geochemistry*. Geological Publishing House, Beijing, China.

Drever J. I. (1974) Geochemical model for origin of Precambrian Iron Formations. *Geol. Soc. Am. Bull.* **85**, 1099–1106.

Ehrenreich A. and Widdel F. (1994) Anaerobic oxidation of ferrous iron by purple bacteria, a new-type of phototrophic metabolism. *Appl. Environ. Microbiol.* **60**, 4517–4526.

Eriksson P. G., Catuneanu O., Sarkar S. and Tirsgaard H. (2005) Patterns of sedimentation in the Precambrian. *Sediment. Geol.* **176**, 17–42.

Ewers W. E. and Morris R. C. (1981) Studies of the Dales Gorge member of the Brockman iron formation, Western Australia. *Econ. Geol.* **76**, 1929–1953.

Fischer W. W. and Knoll A. H. (2009) An iron shuttle for deepwater silica in Late Archean and early Paleoproterozoic iron formations. *GSA Bull.* **121**, 222–235.

Fischer W. W., Schroeder S., Lacassie J. P., Beukes N. J., Goldberg T., Strauss H., Horstmann U. E., Schrag D. P. and Knoll A. H.

(2009) Isotopic constraints on the Late Archean carbon cycle from the Transvaal Supergroup along the western margin of the Kaapvaal craton, South Africa. *Precambrian Res.* **169**, 15–27.

Frost C. D., von Blanckenburg F., Schoenberg R., Frost B. R. and Swapp S. M. (2007) Preservation of Fe isotope heterogeneities during diagenesis and metamorphism of banded iron formation. *Contrib. Mineral. Petrol.* **153**, 211–235.

Georg R. B., Reynolds B. C., Frank M. and Halliday A. N. (2006) Mechanisms controlling the silicon isotopic compositions of river waters. *Earth Planet. Sci. Lett.* **249**, 290–306.

Georg R. B., West A. J., Basu A. R. and Halliday A. N. (2009) Silicon fluxes and isotope composition of direct groundwater discharge into the Bay of Bengal and the effect on the global ocean silicon isotope budget. *Earth Planet. Sci. Lett.* **283**, 67–74.

Gutzmer J., Beukes N. J., De Kock M. O. and Netshiozwi S. T. (2005) Origin of high-grade iron ores at the Thabazimbi deposit, South Africa. *Iron Ore Conference, Freemantle, 19–21 September 2005, Proceedings*, pp. 57–65.

Hamade T., Konhauser K., Raiswell R., Goldsmith S. and Morris R. (2003) Using Ge/Si ratios to decouple iron and silica fluxes in Precambrian banded iron formations. *Geology* **31**, 35–38.

Han T. (1978) Microstructures of magnetite as guide to its origin in some Precambrian iron formations. *Fortschr. Mineral.* **56**, 105–142.

Handler R. M., Beard B. L., Johnson C. M. and Scherer M. M. (2009) Atom exchange between aqueous Fe(II) and goethite: an Fe isotope tracer study. *Environ. Sci. Technol.* **43**, 1107–1109.

Holland H. D. (1973) Ocean – possible source of iron in iron-formations. *Econ. Geol.* **68**, 1169–1172.

Homoky W. B., Severmann S., Mills R. A., Statham P. J. and Fones G. R. (2009) Pore-fluid Fe isotopes reflect the extent of benthic Fe redox recycling: evidence from continental shelf and deep-sea sediments. *Geology* **37**, 751–754.

Horn I. and von Blanckenburg F. (2007) Investigation on elemental and isotopic fractionation during 196 nm femtosecond laser ablation multiple collector inductively coupled plasma mass spectrometry. *Spectrochim. Acta B* **62**, 410–422.

Horn I., von Blanckenburg F., Schoenberg R., Steinhoefel G. and Markl G. (2006) In situ iron isotope ratio determination using UV-femtosecond laser ablation with application to hydrothermal ore formation processes. *Geochim. Cosmochim. Acta* **70**, 3677–3688.

Isley A. E. (1995) Hydrothermal plumes and the delivery of iron to banded iron formation. *J. Geol.* **103**, 169–185.

Isley A. E. and Abbott D. H. (1999) Plume-related mafic volcanism and the deposition of banded iron formation. *J. Geophys. Res.* **104**, 15461–15477.

Jacobsen S. B. and Pimentel-Klose M. R. (1988) Nd isotopic variations in Precambrian banded iron formations. *Geophys. Res. Lett.* **15**, 393–396.

Jang J. H., Mathur R., Liermann L. J., Ruebush S. and Brantley S. L. (2008) An iron isotope signature related to electron transfer between aqueous ferrous iron and goethite. *Chem. Geol.* **250**, 40–48.

Jiang S. Y., Ding T. P., Wan D. F. and Li Y. H. (1993) Silicon isotopic compositions of Archean banded Si–Fe Formation (BIF) in the Gongchangling Ore Deposit, Liaoning-Province, China. *Chin. Sci. Bull. B* **36**, 482–489.

Johnson C. M., Beard B. L., Beukes N. J., Klein C. and O'Leary J. M. (2003) Ancient geochemical cycling in the Earth as inferred from Fe isotope studies of banded iron formations from the Transvaal Craton. *Contrib. Mineral. Petrol.* **144**, 523–547.

Johnson C. M., Roden E. E., Welch S. A. and Beard B. L. (2005) Experimental constraints on Fe isotope fractionation during magnetite and Fe carbonate formation coupled to dissimilatory hydrous ferric oxide reduction. *Geochim. Cosmochim. Acta* **69**, 963–993.

Johnson C. M., Beard B. L., Klein C., Beukes N. J. and Roden E. E. (2008a) Iron isotopes constrain biologic and abiologic processes in banded iron formation genesis. *Geochim. Cosmochim. Acta* **72**, 151–169.

Johnson C. M., Beard B. L. and Roden E. E. (2008b) The iron isotope fingerprints of redox and biogeochemical cycling in the modern and ancient Earth. *Annu. Rev. Earth Planet. Sci.* **36**, 457–493.

Kappler A., Pasquero C., Konhauser K. O. and Newman D. K. (2005) Deposition of banded iron formations by anoxygenic phototrophic Fe(II)-oxidizing bacteria. *Geology* **33**, 865–868.

Kaufman A. J. (1996) Geochemical and mineralogic effects of contact metamorphism on banded iron-formation: an example from the Transvaal Basin, South Africa. *Precambrian Res.* **79**, 171–194.

Kaufman A. J., Hayes J. M. and Klein C. (1990) Primary and diagenetic controls of isotopic compositions of iron-formation carbonates. *Geochim. Cosmochim. Acta* **54**, 3461–3473.

Kaufman A. J., Johnston D. T., Farquhar J., Masterson A. L., Lyons T. W., Bates S., Anbar A. D., Arnold G. L., Garvin J. and Buick R. (2007) Late Archean biospheric oxygenation and atmospheric evolution. *Science* **317**, 1900–1903.

Klein C. (2005) Some Precambrian banded iron-formations (BIFs) from around the world: their age, geologic setting, mineralogy, metamorphism, geochemistry, and origin. *Am. Mineral.* **90**, 1473–1499.

Klein C. and Beukes N. J. (1989) Geochemistry and sedimentology of a facies transition from limestone to iron-formation deposition in the early Proterozoic Transvaal Supergroup, South Africa. *Econ. Geol.* **84**, 1733–1774.

Knauth, A. H. (1994) Petrogenesis of chert. In *Silica: Physical Behaviour, Geochemistry, and Materials Applications*, vol. 29 (eds. P. J. Heaney, C. T. Prewitt and G. V. Gibbs). Reviews in Mineralogy, Mineralogical Society of America. pp. 233–258.

Konhauser K. O., Lalonde S. V., Amskold L. and Holland H. D. (2007a) Was there really an Archean phosphate crisis? *Science* **315**, 1234.

Konhauser K. O., Amskold L., Lalonde S. V., Posth N. R., Kappler A. and Anbar A. (2007b) Decoupling photochemical Fe(II) oxidation from shallow-water BIF deposition. *Earth Planet. Sci. Lett.* **258**, 87–100.

Konhauser K. O., Hamade T., Raiswell R., Morris R. C., Ferris F. G., Southam G. and Canfield D. E. (2002) Could bacteria have formed the Precambrian banded iron formations? *Geology* **30**, 1079–1082.

Lovley D. R. (1991) Dissimilatory Fe(III) and Mn(IV) reduction. *Microbiol. Rev.* **55**, 259–287.

Maliva R. G., Knoll A. H. and Simonson B. M. (2005) Secular change in the Precambrian silica cycle: insights from chert petrology. *Geol. Soc. Am. Bull.* **117**, 835–845.

Mikutta C., Wiederhold J. G., Cirpka O. A., Hofstetter T. B., Bourdon B. and Von Gunten U. (2009) Iron isotope fractionation and atom exchange during sorption of ferrous iron to mineral surfaces. *Geochim. Cosmochim. Acta* **73**, 1795–1812.

Mineev S. D., Polyakov V. B. and Permyakov Y. V. (2007) Equilibrium iron isotope fractionation factors for magnetite from Mössbauer spectroscopy and inelastic nuclear resonant X-ray scattering data. *Geochim. Cosmochim. Acta* **71**, A669.

Miyano T. and Beukes N. J. (1984) Phase relations of stilpnomelane, ferri-annite and riebeckite in very low-grade metamorphosed iron-formations. *Trans. Geol. Soc. S. Afr.* **87**, 111–124.

Morris R. C. (1993) Genetic modelling for banded iron-formation of the Hamersley Group, Pilbara Craton, Western Australia. *Precambrian Res.* **60**, 243–286.

Mücke A. (2003) General and comparative considerations of whole-rock and mineral compositions of Precambrian iron-formations and their implications. *J. Miner. Abh.* **179**, 175–219.

Nelson D. R., Trendall A. F. and Altermann W. (1999) Chronological correlations between the Pilbara and Kaapvaal cratons. *Precambrian Res.* **97**, 165–189.

Ohmoto H. (2003) Nonredox transformation of magnetite–hematite in hydrothermal systems. *Econ. Geol.* **98**, 157–161.

Pecoits E., Gingras M. K., Barley M. E., Kappler A., Posth N. R. and Konhauser K. O. (2009) Petrography and trace element geochemistry of Dales Gorge banded iron formation: paragenetic sequence, source and implications for palaeo-ocean chemistry. *Precambrian Res.* **172**, 163–197.

Pedersen H. D., Postma D., Jakobsen R. and Larsen O. (2005) Fast transformation of iron oxyhydroxides by the catalytic action of aqueous Fe(II). *Geochim. Cosmochim. Acta* **69**, 3967–3977.

Perry E. C. and Lefticariu L. (2003) Formation and geochemistry of Precambrian chert. In *Treatise on Geochemistry* (ed. F. T. Mackenzie). Elsevier, Amsterdam. pp. 99–113.

Pickard A. L. (2002) SHRIMP U–Pb zircon ages of tuffaceous mudrocks in the Brockman Iron Formation of Hamersley Range, Western Australia. *Aust. J. Earth Sci.* **49**, 491–507.

Pickard A. L. (2003) SHRIMP U–Pb zircon ages for the Palaeoproterozoic Kuruman Iron Formation, Northern Cape Province, South Africa: evidence for simultaneous BIF deposition on Kaapvaal and Pilbara Cratons. *Precambrian Res.* **125**, 275–315.

Polyakov V. B. and Mineev S. D. (2000) The use of Mössbauer spectroscopy in stable isotope geochemistry. *Geochim. Cosmochim. Acta* **64**, 849–865.

Polyakov V. B., Clayton R. N., Horita J. and Mineev S. D. (2007) Equilibrium iron isotope fractionation factors of minerals: reevaluation from the data of nuclear inelastic resonant X-ray scattering and Mössbauer spectroscopy. *Geochim. Cosmochim. Acta* **71**, 3833–3846.

Robert F. and Chaussidon M. (2006) A palaeotemperature curve for the Precambrian oceans based on silicon isotopes in cherts. *Nature* **443**, 969–972.

Rouxel O. J., Bekker A. and Edwards K. J. (2005) Iron isotope constraints on the Archean and Paleoproterozoic ocean redox state. *Science* **307**, 1088–1091.

Severmann S., Johnson C. M., Beard B. L. and McManus J. (2006) The effect of early diagenesis on the Fe isotope compositions of porewaters and authigenic minerals in continental margin sediments. *Geochim. Cosmochim. Acta* **70**, 2006–2022.

Severmann S., Lyons T. W., Anbar A., McManus J. and Gordon G. (2008) Modern iron isotope perspective on the benthic iron shuttle and the redox evolution of ancient oceans. *Geology* **36**, 487–490.

Sharpe M. R. and Chadwick B. (1982) Structures in Transvaal Sequence rocks within and adjacent to the eastern Bushveld Complex. *Trans. Geol. Soc. S. Afr.* **85**, 29–41.

Siever R. (1992) The silica cycle in the Precambrian. *Geochim. Cosmochim. Acta* **56**, 3265–3272.

Skulan J. L., Beard B. L. and Johnson C. M. (2002) Kinetic and equilibrium Fe isotope fractionation between aqueous Fe(III) and hematite. *Geochim. Cosmochim. Acta* **66**, 2995–3015.

Spotl C. and Vennemann T. W. (2003) Continuous-flow isotope ratio mass spectrometric analysis of carbonate minerals. *Rapid Commun. Mass Spectrom.* **17**, 1004–1006.

Staubwasser M., von Blanckenburg F. and Schoenberg R. (2006) Iron isotopes in the early marine diagenetic iron cycle. *Geology* **34**, 629–632.

Steinhoefel G., Horn I. and Blanckenburg F. (2009a) Micro-scale tracing of Fe and Si isotope signatures in banded iron formation using femtosecond laser ablation. *Geochim. Cosmochim. Acta.* **18**, 5343–5360.

Steinhoefel G., Horn I. and Blanckenburg F. (2009b) Matrix-independent stable Fe isotope ratio determination using UV femtosecond laser ablation ICP-MS. *Chem. Geol.* **268**, 67–73.

Sumner D. Y. (1997) Carbonate precipitation and oxygen stratification in late Archean seawater as deduced from facies and stratigraphy of the Gamohaan and Frisco formations, Transvaal Supergroup, South Africa. *Am. J. Sci.* **297**, 455–487.

Trendall A. (2002) The significance of iron-formation in the Precambrian stratigraphic record. In *Precambrian Sedimentary Environments: A Modern Approach to Depositional Systems*, vol. 33. Special Publication International Association of Sedimentologists. pp. 33–66.

Trendall A. F. and Blockley J. G. (1970) The Iron-Formation of the Precambrian Hamersley Group, Western Australia, with special reference to the associated crocidolite. *Bull. Geol. Surv. W. Aust.* **119**, 366 pp.

Trendall A. F., Compston W., Nelson D. R., De Laeter J. R. and Bennett V. C. (2004) SHRIMP zircon ages constraining the depositional chronology of the Hamersley Group, Western Australia. *Aust. J. Earth Sci.* **51**, 621–644.

Valaas Hyslop E., Valley J. W., Johnson C. M. and Beard B. L. (2008) The effects of metamorphism on O and Fe isotope compositions in the Biwabik iron-formation, northern Minnesota. *Contrib. Mineral. Petrol.* **155**, 313–328.

van den Boorn S. H. J. M., van Bergen M. J., Nijman W. and Vroon P. Z. (2007) Dual role of seawater and hydrothermal fluids in Early Archean chert formation: evidence from silicon isotopes. *Geology* **35**, 939–942.

van den Boorn S. H. J. M., van Bergen M. J., Vroon P. Z., Vries S. T. and Nijman W. (2010) Silicon isotope and trace element constraints on the origin of ~3.5 Ga cherts: implications for early Archean marine environments. *Geochim. Cosmochim. Acta.* **74**, 1077–1103.

von Blanckenburg F., Mamberti M., Schönberg R., Kamber B. S. and Webb G. E. (2008) The iron isotope composition of microbial carbonate. *Chem. Geol.* **249**, 113–486.

Veizer J., Hoefs J., Ridler R. H., Jensen L. S. and Lowe D. R. (1989) Geochemistry of Precambrian carbonates: I. Archean hydrothermal systems. *Geochim. Cosmochim. Acta* **53**, 845–857.

Walraven F., Armstrong R. and Kruger F. (1990) A chronostratigraphic framework for the north-central Kaapvaal craton, the Bushveld Complex and the Vredefort structure. *Tectonophysics* **171**, 23–48.

Welch S. A., Beard B. L., Johnson C. M. and Braterman P. S. (2003) Kinetic and equilibrium Fe isotope fractionation between aqueous Fe(II) and Fe(III). *Geochim. Cosmochim. Acta* **67**, 4231–4250.

Whitehouse M. J. and Fedo C. M. (2007) Microscale heterogeneity of Fe isotopes in >3.71 Ga banded iron formation from the Isua Greenstone Belt, Southwest Greenland. *Geology* **35**, 719–722.

Widdel F., Schnell S., Heising S., Ehrenreich A., Assmus B. and Schink B. (1993) Ferrous iron oxidation by anoxygenic phototrophic bacteria. *Nature* **362**, 834–836.

Wiesli R. A., Beard B. L. and Johnson C. M. (2004) Experimental determination of Fe isotope fractionation between aqueous Fe(II), siderite and "green rust" in abiotic systems. *Chem. Geol.* **211**, 343–362.

Yamaguchi K. E., Johnson C. M., Beard B. L. and Ohmoto H. (2005) Biogeochemical cycling of iron in the Archean–Paleoproterozoic Earth: Constraints from iron isotope variations in sedimentary rocks from the Kaapvaal and Pilbara Cratons. *Chem. Geol.* **218**, 135–169.

Ziegler K., Chadwick O. A., Brzezinski M. A. and Kelly E. F. (2005) Natural variations of d30Si ratios during progressive basalt weathering, Hawaiian Islands. *Geochim. Cosmochim. Acta* **69**, 4597–4610.

Associate editor: David R. Cole